Self-Standing Graphene Papers Decorated with Metal Oxide Nanostructures: Preparation and Application in Electrochemical Capacitors

by

Tuğçe Beyazay

A thesis Submitted to the Graduate School of Sciences and Engineering in Partial Fulfillment of the Requirements for the Degree of Master of Science

in

Materials Science and Engineering

KOÇ
ÜNİVERSİTESİ

February 2019

ABSTRACT

Due to depletion of fossil fuels and global warming, there is an increasing need for clean and renewable energy as well as efficient energy storage technologies. Energy storage systems such as batteries and supercapacitors are required for balanced and continuous power supplies. Electrochemical Capacitors have received great attention due to their high energy density and high charge-discharge efficiency. Electrode material plays an important role in the performance of energy storage devices. Therefore, proper construction of electrode materials composed of highly conductive current collectors and nanostructured active materials are crucial for full utilization of the device performance.

In this thesis, graphene paper and metal oxide composites are prepared as self-standing and flexible electrodes for electrochemical capacitors. For this purpose, graphene oxide paper is obtained from graphene oxide solution synthesized via Hummers' method. Reduction of graphene oxide paper is performed via chemical reduction and thermal annealing. Effects of different reduction techniques on the morphology and electrochemical properties are examined. Then, cathodic electrodeposition of manganese oxide onto reduced graphene oxide paper is carried out to prepare flexible and binder-free electrodes for electrochemical capacitors. Effects of electrodeposition potential and the amount of deposited mass on the electrochemical performance are examined. Hausmannite phase manganese oxide coated electrodes exhibit promising performance in charge-discharge and cyclic voltammetry measurements with specific capacitance of 546 F g^{-1} at current density of 0.5 A g^{-1} and 308 F g^{-1} at scan rate of 1 mV s^{-1}, respectively. During potential cycling, phase transformation of Mn_3O_4 to mixed-valent MnO_x is observed. Consequently, MnO_x nanostructures on self-standing reduced graphene oxide electrodes have 154% capacitance retention at 10000 cycles of cyclic voltammetry. Lastly, superparamagnetic iron oxide nanoparticles decorated reduced graphene oxide papers are prepared via two different methods. Increasing the amount of iron oxide

nanoparticles on the graphene papers results in enhanced capacitance, as expected. In the galvanostatic charge-discharge measurements, Fe_3O_4/rGO electrode exhibits specific capacitance of 203 F g^{-1} at 0.5 mA cm^{-2}. This value is remarkable since the electrode has a high weight of 2 mg cm^{-2}, which shows that the electrode can be used for practical purposes. Moreover, Fe_3O_4/rGO electrodes achieves wide working potential window of 1.6 V (in aqueous electrolyte) and high capacitance retention of 78% at 10000 cycles.

ÖZET

Küresel ısınma ve fosil yakıtların hızla tükenmesinden dolayı yenilenebilir enerjiye olan ihtiyaç artış göstermektedir. Piller ve super kapasitörler gibi enerji depolama sistemleri dengeli ve düzenli güç sağlamak için gereklidir. Elektrokimyasal kapasitörler yüksek güç yoğunlukları ve hızlı şarj-deşarj özellikleri sayesinde son yıllarda popülerlik kazanmışlardır. Elektrot malzemeleri super kapasitörlerin elektrokimyasal performansları üzerinde önemli etkiye sahiptir. Bu nedenle, iletken akım toplayıcılardan ve nano-yapılı aktif malzemelerden oluşan elektrot malzemelerinin düzgün bir araya getirilmesi, sistem performansından maksimum yararlanabilmek için son derece önemlidir.

Bu çalışmada, grafen ile metal oksitlerin kompozitleri hazırlanılarak kendi kendine durabilen ve esnek elektrotlar elde edilmiştir. Bu amaçla, grafen oksit elektrotları modifiye Hummers yöntemi ile sentezlenen grafen oksit solüsyonundan elde edilmiştir. Grafen oksit elektrotlar kimyasal ve termal tavlama yöntemleri kullanılarak indirgenmiştir. Farklı indirgeme yöntemlerinin morfoloji ve elektrokimyasal özellikler üzerindeki etkileri incelenmiştir. Daha sonra, esnek ve kendi kendine durabilen elektrotlar elde etmek için mangan oksit filmler indirgenmiş grafen oksit elektrotlar üzerinde katodik elektrodepozisyon yöntemi ile büyütülmüştür. Elektrodepozisyon potansiyeli ve kaplanan mangan oksit miktarının morfolojik ve elektriksel özellikler üzerindeki etkisi incelenmiştir. Kaplanan mangan oksit Hausmannite fazı çevrimsel voltametri ve şarj/deşarj ölçümleri sırasında yüksek performans göstermiştir. Mangan oksit kaplı elektrotlar, şarj/deşarj ve çevrimsel voltametri ölçümlerinde sırasıyla 546 $F\,g^{-1}$ (0.5 $A\,g^{-1}$ akım yoğunluğunda) ve 308 $F\,g^{-1}$ (1 $mV\,s^{-1}$ tarama hızında) gibi umut vadeden kapasitif performans göstermişlerdir. Çevrimsel voltametri sırasında, mangan oksitin Hausmannite fazından karışık değerlikteki MnO_x fazına dönüştüğü gözlemlenmiştir. Sonuç olarak, kendi kendine durabilen indirgenmiş grafen oksit elektrotları üzerinde biriktirilmiş MnO_x nano yapıları, 10000 çevirim sonunda ilk kapasitans değerinin %154'ünü korumuştur.

Son olarak, süperparamanyetik demir oksit nanopartikülleri ve indirgenmiş grafen oksit kompozitleri iki farklı yöntem ile hazırlanmıştır. Demir oksit miktarının kompozit yapısında arttırılmasıyla spesifik kapasitans değerlerinin beklendiği gibi yükseldiği gözlemlenmiştir. Şarj/deşarj analizleri sonucunda 0.5 mA cm^{-2} akım yoğunluğunda 203 F g^{-1} deşarj kapasitesi elde edilmiştir. Bu değer 2 mg ağırlığındaki bir elektrot için yüksektir ve bu elektrotlar pratik uygulama alanlarında kullanılabilir. Ayrıca, üretilen demir oksit/ indirgenmiş grafen oksit kompozit elektrotları sulu elektrolit içinde geniş potansiyel aralıkta çalışabilmektedirler (1.6 V) ve 10000 çevirim sonucunda başlangıçtaki kapasitans değerinin %78'i korunmuştur.

ACKNOWLEDGEMENTS

First, I would like to express my sincere heartfelt thanks to my advisor Assoc. Prof. Uğur Ünal for providing me the knowledge of research and supporting me during these 2.5 years. He was always patient and positive. He provided many insightful discussions, suggestions about the research and encouraged me all the time. I am grateful for the opportunity to work in his laboratory.

I wish to thank Dr. F. Eylül Saraç Öztuna for being not only a great labmate but a better friend. She knows all questions and answers. I cannot forget our demo Skype interviews. She has been a lifesaver for me since 2015. Thanks for her valuable words of guidance and motivation.

I also would like to thank my labmates Dr. Ceren Yılmaz Akkaya, Dr. Mohammadreza Khobadaskh, Tolga Koçer, and Esra Binici for their endless support and friendship. I couldn't complete this thesis without Eylül, Tolga, Esra, and Tolga's Ankara songs. I am really happy to be a part of this research group.

I wish to thank my flatmate Çiğdem Altıntaş (Çido) who has the kindest heart. I also would like to thank my friends Betül Şeker, Samira Fatma Kurtoğlu, Dr. Melike Babucci (KÜTEM girls), and Ceren Zor for their friendship and cheerful mode during these 2 years.

I would like to thank all members of Materials Science and Engineering department who supported me directly or indirectly in the progress of my research work.

I wish to thank my best friends İrem Ülkü and Ezgi Kısa for being wonderful friends.

Lastly, I would like to express my thanks to loving members of my family.

This study is dedicated to my beloved aunt, Emine Beyazay (Canım Halam), who is the person of motivation in my life.

TABLE OF CONTENTS

LIST OF TABLES

LIST OF FIGURES

LIST OF ACRONYMS

APTMS: 3-(Aminopropyl) trimethoxysilane

CV: Cyclic voltammetry

ECs: Electrochemical capacitors

EDLC: Electrical double layer capacitor

EIS: Electrochemical impedance spectroscopy

ESR: Equivalent series resistance

FESEM: Field-Emission scanning electron microscopy

GCD: Galvanostatic charge-discharge

GO: Graphene oxide

rGO: Reduced graphene oxide

SPION: Superparamagnetic iron oxide nanoparticles

XPS: X-ray photoelectron spectroscopy

XRD: X-ray diffraction

Chapter 1: Introduction

1.1. Graphene and Its Derivatives

Graphene consists of a one-atom-thick sheet of sp^2-bonded carbon atoms arranged in a hexagonal lattice, which is attracting tremendous attention in the field of material science because of its exceptional physicochemical properties. It has good electrical conductivity, ultra-high theoretical specific surface area (2630 $m^2 g^{-1}$) [1], high mechanical strength with excellent flexibility, which are highly propitious for flexible devices. Graphene is also known as the mother of carbon-based materials such as fullerenes, carbon nanotubes, and graphite [2]. Natural graphite has stacked graphene layers with π - π stacking interactions, which provide high thermodynamic stability to graphite. There are several methods including mechanical exfoliation of pyrolytic graphite (scotch-tape method), which is also the first isolation method of single-layer graphene honored with the Nobel Prize in Physics in 2010 [3], chemical vapor deposition [4], thermal decomposition of silicon carbide in ultra-high vacuum condition [5], mild exfoliation of graphite [6], thermal and chemical reduction of graphite oxide to obtain graphene sheets. Ideal graphene should be perfectly flat with trigonally connected sp^2-hybridized carbons [7].

1.1.1. Graphene Oxide

Graphene oxide, a single layer of graphite oxide, is often used as a precursor for graphene synthesis. The most known way to produce graphite oxide, precursor of graphene oxide, is the oxidation of graphite. Decades ago, Brodie [8], Staudenmeir, and Hummers *et al.* [9] developed the first methods for the synthesis of graphite oxide and these methods are still most popular approaches towards graphite oxide synthesis with minor modifications [10]. Both Brodie and Staudenmeier use $KClO_3$ and HNO_3 to oxidize the graphite and they generate hazardous ClO_2 gas, which can rapidly decompose in air and may cause explosions [11]. Currently, Hummers' method is commonly used due to its relatively shorter reaction time and the absence of ClO_2

gas. The main drawback of Hummers' method is the contamination caused by permanganate ions, which can be removed by H_2O_2 addition and washing with water [11]. Although the complete reaction pathway is unclear, Dreyer *et al*. [12] claimed that Mn_2O_7 was the active species. Additionally, Dimiev and Tour studied the formation mechanism of graphene oxide [13]. The main species which lead to oxidation of graphite are MnO_3^+ and Mn_2O_7 which are products of the reaction between $KMnO_4$ and H_2SO_4 according to following equation:

$$KMnO_4 + 3H_2SO_4 \rightarrow K^+ + MnO_3^+ \; 3HSO_4^-$$

$$MnO_3^+ + \; MnO_4^- \rightarrow Mn_2O_7$$

The oxidation of graphite results in formation of defects in stacked graphene sheets because it breaks up sp^2-hybridized carbon network. Moreover, the nature of functional groups in graphene oxide highly depends on the reaction conditions, including reaction time, and temperature [14]. The oxidation process also increases the distance between graphene sheets from 0.35 nm to 0.8 nm due to the intercalation of water molecules within the stacked sheets. This intercalation enables delamination of graphite oxide sheets to individual graphene oxide nanosheets with the aid of sonication. Although the precise structure of graphene oxide nanosheet is still uncertain, NMR study of ^{13}C-labelled graphene oxide conducted by Cai *et al.* [15] supports the model of He and Lerf *et al.* [16,17] in which the plane of graphene sheet is decorated with carbonyl, epoxy, and hydroxyl functional groups (Figure 1-1) . These functional groups facilitate the surface-modification reactions, which help developing functionalized graphene-based materials for various applications such as field-effect transistors [18], capacitors [19], and lithium-ion batteries [11]. Oxygen-containing groups on graphene oxide can also facilitate faradaic reactions on the surface, which enhance electrochemical performance of graphene [20]. Furthermore, the polar oxygen functional groups make graphene oxide highly hydrophilic, which provides dispersibility in many different solvents, especially in water [21]. Resultant graphene oxide dispersion can be directly utilized in electrode

preparation methods such as spin coating [22], drop casting [23], dip coating [24], spraying [25], or vacuum filtration [26]. Due to the existence of several oxygenated functional groups, "as-synthesized" graphene oxide has various interesting properties such as thermal, mechanical, electrochemical properties, and chemical reactivity [21]. Chemical and atomic structure of GO sheets strongly affects its electronics properties. GO film is intrinsically an insulator with a sheet resistance value (R_s) about 10^{12} ohm sq^{-1} [27]. Its insulating character is highly associated with the amount of sp^3-hybridized C atoms [21]. Additionally, GO displays enhanced chemical reactivity compared to graphite because of the presence of structural defects and oxygenated functional groups.

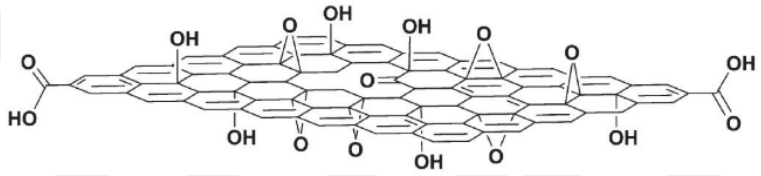

Figure 1-1: Schematic illustration of graphene oxide [11]

Table 1-1. Methods for graphite oxidation [6]

Method	Oxidants	Reaction Time	Intersheet Distance	C:O Ratio
Brodie	$KClO_3$, HNO_3	3-4 days	0.59 nm	2.28
Staudenmaier	$KClO_3$, HNO_3, H_2SO_4	10 days	0.62 nm	1.85
Hummers	$NaNO_3$, $KMnO_4$, H_2SO_4	9-10 hours	0.67 nm	2.17

1.1.2. Reduced graphene oxide

Among aforementioned graphene production methods, graphene from GO reduction was utilized for most of electrochemical applications [28]. Furthermore, this method is considered as an economical way to mass-produce graphene sheets [1]. While the addition of oxygenated groups during the oxidation of graphite facilitates dispersion of graphene oxide in water, these functional groups decrease the sheet conductivity. Deoxygenation of graphene oxide provides the partial recovery of graphene structure and the π-electron conjugation is partially restored in

the graphitic skeleton. The resulted reduced GO resembles graphene with oxygenated groups and structural defects [2]. There are several methods reported for the reduction of GO including chemical reduction [29], thermal reduction [30], photo-chemical [31], microwave-assisted [32], and electrochemical reduction [33]. In thermal reduction, annealing atmosphere and the temperature are the key parameters. Thermal annealing can be performed in an inert [20], vacuum [34], or reducing atmosphere [35]. Thermal-energy-induced multistep removal of oxygen containing functional groups including carboxyl, hydroxyl, epoxy and the intercalated H_2O molecules is carried out during thermal annealing [2]. While chemical reduction leads to the reduction of individual GO sheets in the solution by a strong base, thermal annealing provides rapid heating and exfoliation of stacked graphite sheets. The main drawback of thermal annealing is the large energy consumption and it cannot be utilized for films deposited on substrates which have low-melting points [36]. Chemical reduction results in increase hydrophobicity and π-stacking interactions between graphene sheets. Earlier works prove that deoxygenation of graphene oxide can be successfully performed through chemical reduction with sodium borohydride [37], L-ascorbic acid [38], hydrogen iodide [39], urea [40], and hydrazine [41]. The chemical reduction of GO does not require complex equipment, so chemical reduction is an easier and cheaper way to produce graphene. The first study of the chemical reduction with hydrazine hydrate was reported by Stankovich *et al.* [42], who proposed the reduction mechanism by hydrazine given in Figure 1-2. According to their report, the ring-opening of epoxy groups by hydrazine leads to the formation of hydrazino alcohols NH_2NH_2, which fasten the reduction process. Kim *et al.* [43] conducted DFT calculations of epoxide reduction with hydrazine on graphene layer, which proved that the epoxy ring opening governs the reduction reaction. Furthermore, Gao *et al.* also reported DFT simulations, which claims that only epoxy groups are reduced during hydrazine reduction, while there is no reaction pathway for the reduction of carboxyl, hydroxyl, or carbonyl groups [44]. In summary, the

advantage of chemical reduction is the removal of functional groups without destroying the carbon plane while the thermal annealing at high temperatures enhances the removal of various functional groups.

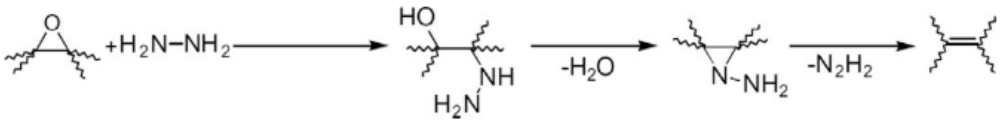

Figure 1-2 The proposed reaction mechanism of epoxide ring opening with hydrazine reduction [42]

1.2. Electrochemical Capacitors

With increasing world population, renewable and environment friendly energy storage systems play a significant role in wide range of industrial applications [45]. Fuel cells, batteries, and supercapacitors are among the most effective and practical systems for energy storage. Recently, supercapacitors, also known as ultracapacitors or electrochemical capacitors, have gained significant attention due to their long cycle life, high power density, and fast charge-discharge characteristics. Main advantages of supercapacitors over fuel cells and batteries are their wide range of operating temperature and long service life [46]. However, supercapacitors have relatively low energy density compared to batteries and fuel cells (Figure 1-3) [47]. To overcome the problem, the development of new materials for supercapacitor electrodes has attracted much attention. A supercapacitor device is similar to batteries in design, it comprises of two electrodes, an electrolyte, and a separator which isolates electrodes electrically. According to the mechanism of energy storage, supercapacitors can be divided into two main categories: Electrical Double Layer Capacitors (EDLCs) and Pseudocapacitors.

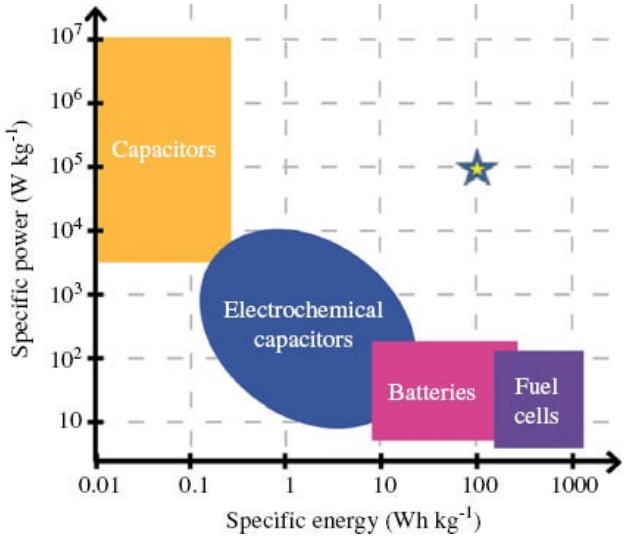

Figure 1-3. Ragone Plot of energy storage and conversion devices.

1.2.1. Electrical Double Layer Capacitors

EDLCs' energy storage mechanism is similar to that of dielectric capacitors [46]. In EDLCs, the capacitance results from the accumulation of electrostatic charge, which is a non-Faradaic process, at the interface between the electrode and the electrolyte. The surface charge generation mechanism occurs via surface dissociation as well as ion adsorption from the defects of crystal lattice and the electrolyte [47]. In EDLCs, there is no charge transfer between the electrode surface and the electrolyte, and they deliver energy quickly.

In 1853, Helmholtz described the double layer capacitance. Helmholtz claimed that all the charges adsorbed on the electrode surface. This idea was modified by Gouy and Chapman with the addition of the ion mobility in the electrolyte due to electrostatic forces and the diffusion [45].

The specific capacitance of an EDLC can be calculated by the following equation:

$$C_{EDL} = \frac{\varepsilon_r \times \varepsilon_0 \times A}{d}$$

Where A is the electrode surface area, d is the charge separation distance, ε_r and ε_0 are dielectric constants of the electrolyte and the vacuum, respectively.

Since EDLC consists of two electrodes separated by a separator and electrolyte, there is an electrical double layer in the interface between the electrode and the electrolyte at each electrode-surface. Hence, the cell capacitance is calculated according to following equation [48]:

$$\frac{1}{C} = \frac{1}{C_+} + \frac{1}{C_-}$$

The specific capacitance of this type of supercapacitors is affected by the surface area and pore structure of electrode materials. Carbon materials such as graphene, carbon nanotubes, activated carbon, and carbon fibers are utilized as electrode materials in EDLCs because they possess high surface area and high stability [49].

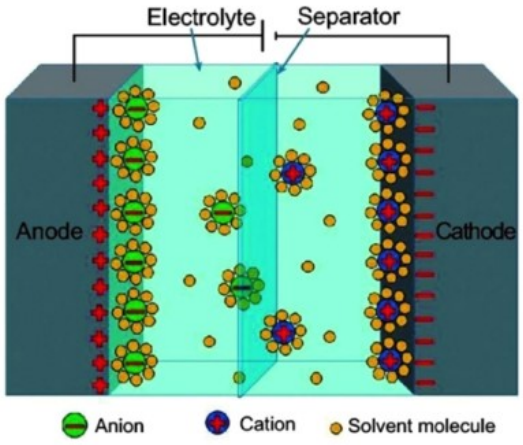

Figure 1-4. Schematic representation of an EDLC [163].

1.2.2. Pseudocapacitors

The new type of electrochemical capacitors, which store energy through electron-transfer mechanism, was discovered in 1971 [50]. The term "pseudocapacitance" is used to describe electrochemical characteristics of electrode materials, which display the signature of capacitive materials such as linear dependence of stored charge with changing potential window, but the charge-storage mechanism does not depend on the accumulation of charges in the electrical double layer [51]. The word "pseudo" means false, fake or almost, approaching. Since the

pseudocapacitive materials show similar behavior with capacitors, the second meaning of "pseudo" is more appropriate in this context. Pseudocapacitors store energy via redox reactions between the electrode and the electrolyte. With an applied potential, fast and reversible Faradaic reactions occur at the surface or near-surface region of electrodes [52]. While EDL capacitance relies on the accumulation of charges, pseudocapacitance is a result of electrochemical charge transfer, which is similar to the charging and discharging processes of batteries [47]. The main difference between batteries and pseudocapacitive materials is their charging-discharging rates. Pseudocapacitors show higher rate capability. Since charging time of pseudocapacitive materials is much less than batteries, they can provide higher power density. Additionally, shorter charging times can be very practical for portable devices. The most promising pseudo-capacitive materials are transition metal oxides such as RuO_2 [53], MnO_2 [54], Fe_3O_4 [55]. Thanks to their multivalent oxidation states. These metal oxides display pseudocapacitive behavior due to the intercalation of alkali metal cations such as Na^+, K^+, Li^+ or protons (H^+) [52]. Chemical reaction does not occur during charging and discharging.

The specific capacitance of pseudocapacitors can be calculated by the following equation:

$$C = \frac{d(\Delta q)}{d(\Delta V)}$$

where q is the charge acceptance of the electrode material, ΔV is the working potential window.

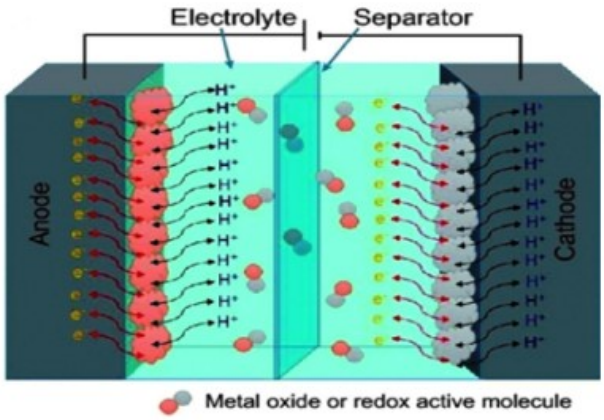

Figure 1-5: Schematic representation of pseudocapacitors [163].

1.2.3. Performance Evaluation of Electrochemical Capacitors

1.2.3.1. Cyclic Voltammetry

An ideal capacitive material displays symmetric cyclic voltammograms at low scan rates during CV measurements. In ideal capacitor case, there is no potential shifts or small potential shifts can occur between the anodic and cathodic peaks (Figure 1-6) [52]. However, deviations from ideal capacitive behavior occurs because of the polarization effects caused by the equivalent series resistance in ECs. In general, pseudocapacitive materials are insulators and there is charge transfer resistance which leads to the kinetic limitations in pseudocapacitors.

While EDLCs show rectangular shape without any deviation with increasing scan rate (Figure 1-6), pseudocapacitors can exhibit rectangular shape with or without peaks, depending on the

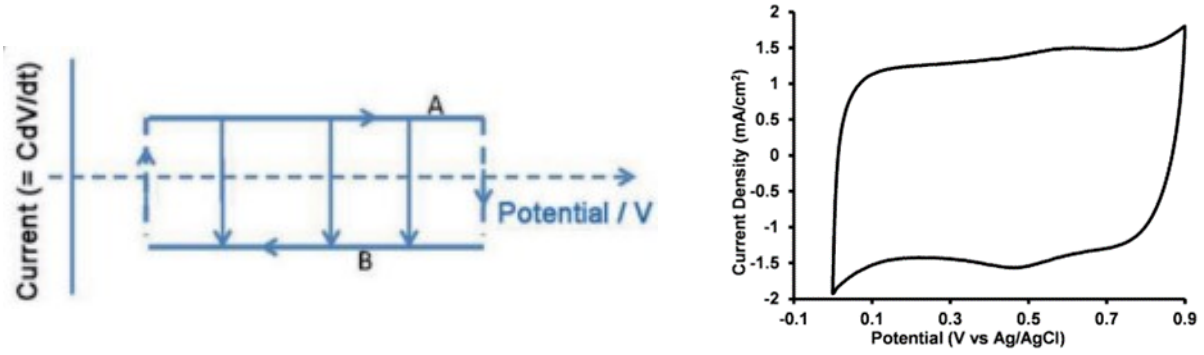

Figure 1-6: CV profiles of ideal EDLC (left) [52], CV curve of manganese oxide film (right) [56].

electrode material. RuO_2 and MnO_2 (Figure 1-6) display nearly ideal rectangular CV curves [52,56].

The difference between anodic and cathodic peak positions in cyclic voltammograms represents the reversibility of electrochemical reactions. While this difference is small for pseudocapacitive materials and does not increase with increasing the scan rate, this difference gets larger in battery-type materials due to the irreversible crystallographic phase transformation reactions and it increases with the increasing scan rate (Figure 1-7). CV is also utilized to distinguish diffusion-controlled and near-surface reactions. To distinguish faradaic and diffusion-controlled reactions, the following equation is used [52]:

$$i(v) = i_c + i_d = av^b$$

where i_c and i_d are capacitive and diffusion- limited kinetic current, respectively. From this equation, the slope of the log i vs log v plot gives coefficient b. If b coefficient is 1, it proves that the near-surface reactions including surface faradaic reactions and fast charge-discharge of EDLC govern the charge storage mechanism. If b coefficient is 0.5, it indicates that the process is diffusion-controlled process, like in batteries.

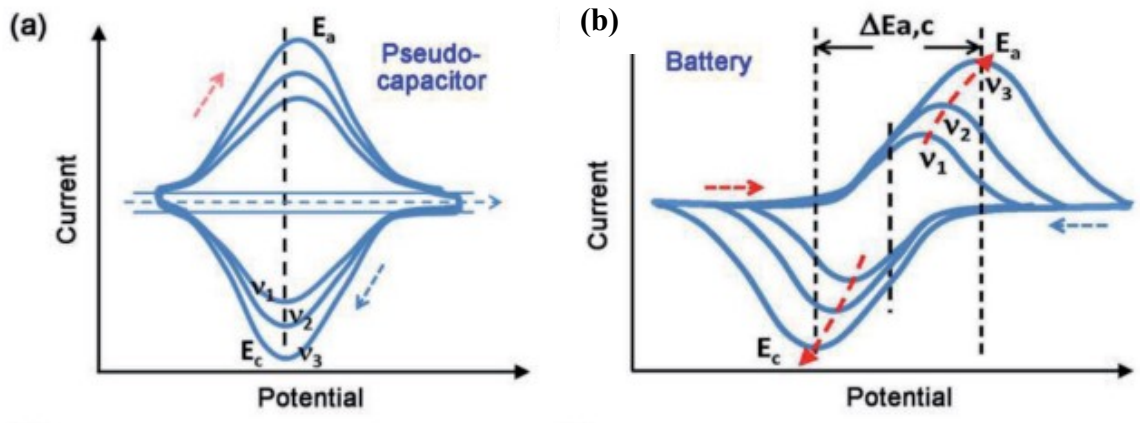

Figure 1-7: Schematic illustration of the cyclic voltammogram behavior of pseudocapacitive material (a) and battery-type material (b) [52]

From the CV curve of ECs, the capacitance can be calculated as [47]:

$$C = \left| \frac{Q}{E_2 - E_1} \right|$$

where Q is the accumulated charge in the electrode layer and is calculated from the area under the cyclic voltammogram, $E_2 - E_1$ is potential difference in either positive direction or negative direction.

Cycle life is another important parameter for performance evaluation of ECs. The stability during the operation is a critical issue and it highly depends on the structural properties of the active materials. Generally, cyclic stability tests are performed with cyclic voltammetry [57–59]

1.2.3.2. Galvanostatic Charge-Discharge

While the shape of potential versus time graph for EDLC is a well-defined linear triangular shape (Figure 1-8a), pseudocapacitors have smooth charge/discharge profiles without plateaus due to the logarithmic function of electrosorbed species (Figure 1-8b). In batteries, there are distinguishable flat discharge plateaus during charging/discharging in potential versus time graph due to phase transformation (Figure 1-8c).

The capacitance of an electrode can be calculated by GCD with following equation [46]:

$$C = \frac{I \times t}{\Delta V}$$

where I is the current density, t is discharge time, and ΔV is potential window.

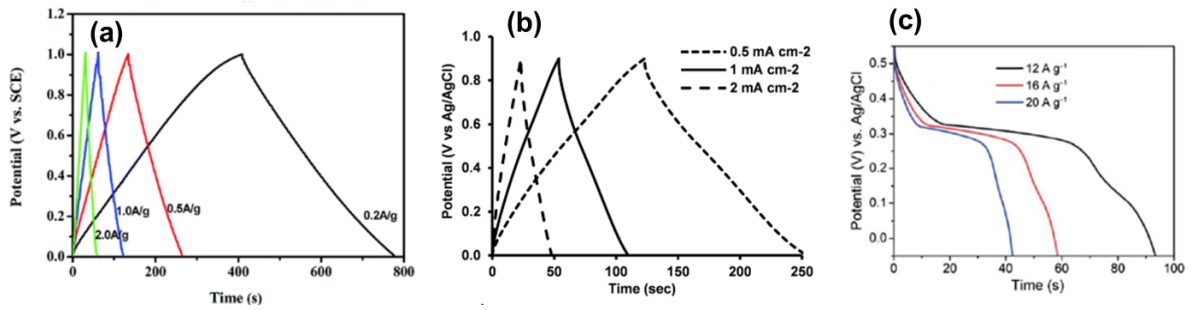

Figure 1-8: Galvanostatic charge-discharge curves of (a) carbon-based EDLC [164], (b) Mn_3O_4 pseudocapacitive material [56], (c) nanostructured Ni $(OH)_2$ electrode which contains both pseudocapacitive and battery-type regions [165].

1.2.3.3. Electrochemical Impedance Spectroscopy

The equivalent series resistance (ESR) is necessary for determining the gravimetric power density of the ECs according to the following equation [60]:

$$P = \frac{1}{4WR_{Cell}}V^2$$

where W is the total weight, V is cell voltage, and R_{cell} is the equivalent series resistance (ESR) of the cell (Ohm).

With decreasing ESR, the power density of the system is increasing. Like other energy storage systems, high ESR values result in low power density and it also affects the charge/discharge rate [60] . Hence, for some applications, ESR is more important than capacitance. ESR is the sum of several contributions such as the resistance of the active material, the resistance of electrolyte with the separator, and the contact resistance between current collector and active material [61].

Electrochemical impedance spectroscopy is an useful tool to characterize the frequency response and to determine the capacitance of ECs [47,61]. It is measured via applying a small amplitude of alternating voltage near the open-circuit potential over a particular frequency range. A Nyquist diagram in which the imaginary part of impedance (Z'') is plotted versus the real part (Z') is utilized to plot experimental data obtained from the measurement. In Nyquist diagram, the diameter of the semicircle gives the charge transfer resistance. The high frequency region which is larger than 10^4 Hz displays the conductivity of the electrolyte and active materials. The information about charge transfer resistance can be obtained from the frequency region of 10^4 to 1 Hz. Finally, low frequency region shows the real capacitive feature. Ideally, a capacitor should exhibit a parallel line to the imaginary axis [47]. Nevertheless, the deviation from the ideal line with an angle between 45°- 90° is observed in real cases. Main reasons for this deviation could be abnormal capacitive behavior due to the pore size distribution or redox

reactions occurring on the surface of the electrode. Furthermore, the Bode plot in which the phase shift is plotted against the frequency can also be utilized to evaluate impedance characteristics [62]. Bode plot indicates that increasing frequency leads to decreasing capacitance because at high frequency regions ECs act as a pure resistor due to the difficulty of ion penetration from electrolyte into micropores.

Chapter 2: Self-Standing and Flexible Reduced Graphene Oxide Papers

2.1. Introduction

Traditional supercapacitors are rigid and unwieldy [63]. In this regard, fabrication of flexible supercapacitors with small volume and light weight has become an emerging field for wearable and portable electronics. In general, a conventional supercapacitor has a two-electrode configuration, which contains metal current collectors such as nickel foam and aluminum foil [64]. Usually, a supercapacitor electrode is prepared by blending active material, binder, and the conductive additive. Unavoidably, the binder and the conductive additive increase the weight of the overall device. Additionally, binders lower the specific capacitance by decreasing the electrical conductivity [65]. Electrode materials with good electrochemical performance, high stability, and excellent mechanical property are necessary for flexible supercapacitors [66,67]. In this regard, carbon-based materials such as graphene, carbon fiber, carbon nanotubes are promising electrode materials for flexible supercapacitor devices due to their large surface area, low weight, high electrochemical stability, and the ease of processability [63,67]. Among carbonaceous materials, graphene is a promising candidate in supercapacitor applications compared to carbon nanotubes, activated carbon, and mesoporous carbon [68]. Graphene has outstanding properties including good (electro)chemical stability, high theoretical specific surface area (2630 m^2 g^{-1}) [69], and excellent electrical conductivity [70]. There are several ways to prepare graphene films including spray coating [71], blade-casting [72], Langmuir-Blodgett assembly [73], chemical vapor deposition [74,75], evaporation of water [76], and vacuum filtration [77–79]. Among these methods, vacuum filtration method is a facile and straightforward technique to obtain self-standing graphene films.

A large number of studies have been carried out on graphene-based flexible supercapacitors. In 2016, Ferrero *et al*. [80]reported preparation of free-standing GO paper via vacuum filtration from the suspension obtained from the oxidation of graphene aerogel. They obtained high areal capacitance of 114 mF cm^{-2} at a current density of 1.2 A cm^{-2}. In 2017, Li *et al.* [81] prepared free-standing porous graphene paper by immersing Cu foil into the colloidal GO solution. They obtained the specific capacitance of 100 F g^{-1} at 100 mV s^{-1}. Recently, He *et al.* [82] fabricated graphene-based paper-like electrode via drop-casting and obtained volumetric capacitance of 3.6 mF cm^{-3} at a current density of 0.5 A cm^{-3}. Moreover, the preparation of three-dimensional paper-like graphene framework as binder-free supercapacitor electrode was reported by Gao *et al*. [83]. The film prepared with polystyrene nanospheres template exhibited a specific capacitance of 95 F g^{-1} at 0.5 A g^{-1} in alkaline electrolyte

In this chapter, self-standing and flexible reduced graphene oxide papers are prepared via simple filtration of colloidal graphene oxide solution synthesized via Modified Hummers' method. To produce reduced GO papers, chemical reduction with hydrazine vapor is carried out. Thermal annealing after chemical reduction is also performed to observe the effect on the structural and electrochemical characteristics. Electrochemical properties of reduced GO papers are evaluated by CV measurements.

2.2. Materials and Methods

2.2.1. Materials

All chemicals were used without further purification. Graphite (natural, 99.9995%), $NaNO_3$ (99%), and Na_2SO_4 were obtained from Alfa Aesar. $KMnO_4$ and H_2O_2 (30%) were obtained from Merck Millipore. HCl (37%), H_2SO_4 (95-97%) and hydrazine monohydrate (98%) were obtained from Sigma Aldrich. Standard Calomel Electrode (SCE, in saturated KCl) was purchased from Radiometer Analytical SAS. Filter papers (cellulose nitrate, 0.45 μm) were obtained from Sartorius Stedim Biolab. All solutions were prepared with doubly distilled water.

2.2.2. Synthesis of Graphene Oxide

Graphene oxide was synthesized via modified Hummers method as reported previously [84]. Graphite powder was oxidized with $KMnO_4$ and $NaNO_3$ in ice-cold concentrated H_2SO_4 solution. First, $KMnO_4$ was added in small portions to the mixture of graphite and $NaNO_3$ in concentrated H_2SO_4. Addition of $KMnO_4$ was slow in order to keep the temperature of the solution below 5 °C. After the addition of $KMnO_4$ was completed, ice-cold water was added slowly keeping the temperature below 40 °C. Then, the reaction was terminated with the addition of water and 30% H_2O_2 after heating the mixture at 75 °C for 30 min. Produced graphite oxide powder was washed with HCl and water and then exfoliated in water via sonication. In order to obtain single layer nanosheet solution, graphite oxide solution was sonicated in ultrasound bath for 4 hours. Resulted solution was centrifuged at 10000 rpm and the nanosheet solution was collected. 5 ml of the solution was filtered via vacuum filtration method in order to find the concentration of the solution. Three papers were filtered and weighed to ensure the exact concentration.

2.2.2.1. Chemical Reduction of Graphene Oxide Paper

Chemical reduction of GO film was performed with hydrazine monohydrate using different reduction times: 6, 10, and 24 h. Self-standing GO paper was placed into a Schott type bottle along with 100 µL hydrazine monohydrate. The bottle was heated to 90 °C.

2.2.2.2. Thermal Reduction of Graphene Oxide Papers Following Chemical Reduction

Thermal reduction of chemically reduced GO papers was performed in a tube furnace. First, rGO papers were placed into furnace and degassed at 110 °C under flowing Ar (200 mL min^{-1}). Then, the temperature was raised to 400 °C under Ar flow. Thermal reduction was carried out for 2 hours. rGO papers were weighed before and after thermal annealing to record the weight loss with Mettler Toledo XP6 microbalance (accuracy of 1 µg).

2.2.3. Structural Characterization of Graphene Oxide and Reduced Graphene Oxide Papers

For the morphological analysis, FESEM (Zeiss Ultra Plus) was used. Defects were evaluated by Raman Spectroscopy (Renishaw Invia) with a 532 nm laser and the laser power was fixed to 0.6 mW to avoid local heating. For each sample, three different measurements were done to ensure reproducibility. Surface chemical structure was analyzed with XPS (Thermo K-Alpha) with an Al Kα source. Fitting of the raw data was performed with Avantage software. XRD patterns were recorded in a range of 2θ degree from 5 to 40° using Bruker D2 diffractometer with a Cu Kα source.

2.2.4. Electrochemical Characterization of Reduced Graphene Oxide Papers

Electrochemical performance of rGO papers was evaluated with cyclic voltammetry in 0.5 M Na_2SO_4 electrolyte. rGO paper, graphite, and SCE were used as working, counter, and reference electrodes, respectively. CV measurements were carried out between the potential window of 0.0-0.8 V vs Ag/AgCl.

2.3. Results and Discussion

2.3.1. Structural Properties of Graphene Oxide and Reduced Graphene Oxide Paper

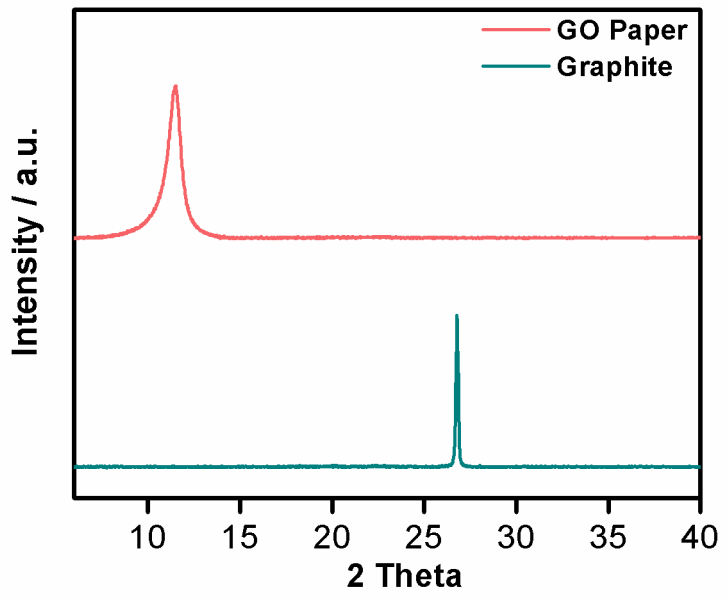

Figure 2-1: XRD patterns of pristine graphite and GO paper.

Prepared GO paper was characterized by XRD. Figure 2-1 displays the XRD patterns of graphite powder and GO paper. The pattern of graphite has a sharp peak at 2θ = 27° which corresponds to 002 plane of graphite [85]. The interlayer spacing is calculated as 0.33 nm according to the following Bragg's law:

$$n\lambda = 2d \sin\theta$$

where θ is the angle of incident X-ray beam, n is the order of diffraction, λ is the X-ray wavelength (Cu-Kα), and d is the interlayer spacing. The XRD pattern of GO has a strong peak at 11.4° which indicates the oxidation of graphite. The interlayer distance is increased to 0.78 nm, which shows that the layers are expanded with the incorporation of oxygen containing functional groups [86].

Reduction of the GO paper with hydrazine vapor resulted in formation of foam-like rGO paper. The color of the free-standing GO paper turned from dark brown to shinny gray and produced rGO papers are flexible and bendable (Figure 2-2a,b and Figure 2-2d,e). Figure 2-2c, and f show cross-sectional FESEM images of self-standing GO and rGO papers. Average thicknesses

of GO and rGO papers are around 1.5 and 120 µm, respectively. Thus, reduction of GO paper results in almost 80-fold increase in the thickness and production of foam-like structure. Effects of chemical reduction time and thermal annealing on the morphology and the thickness of rGO paper are displayed in Figure 2-3. While chemically reduced papers are similar to each other in terms of thickness, thermal annealing results in formation of compact layers and a decrease in the thickness of rGO paper.

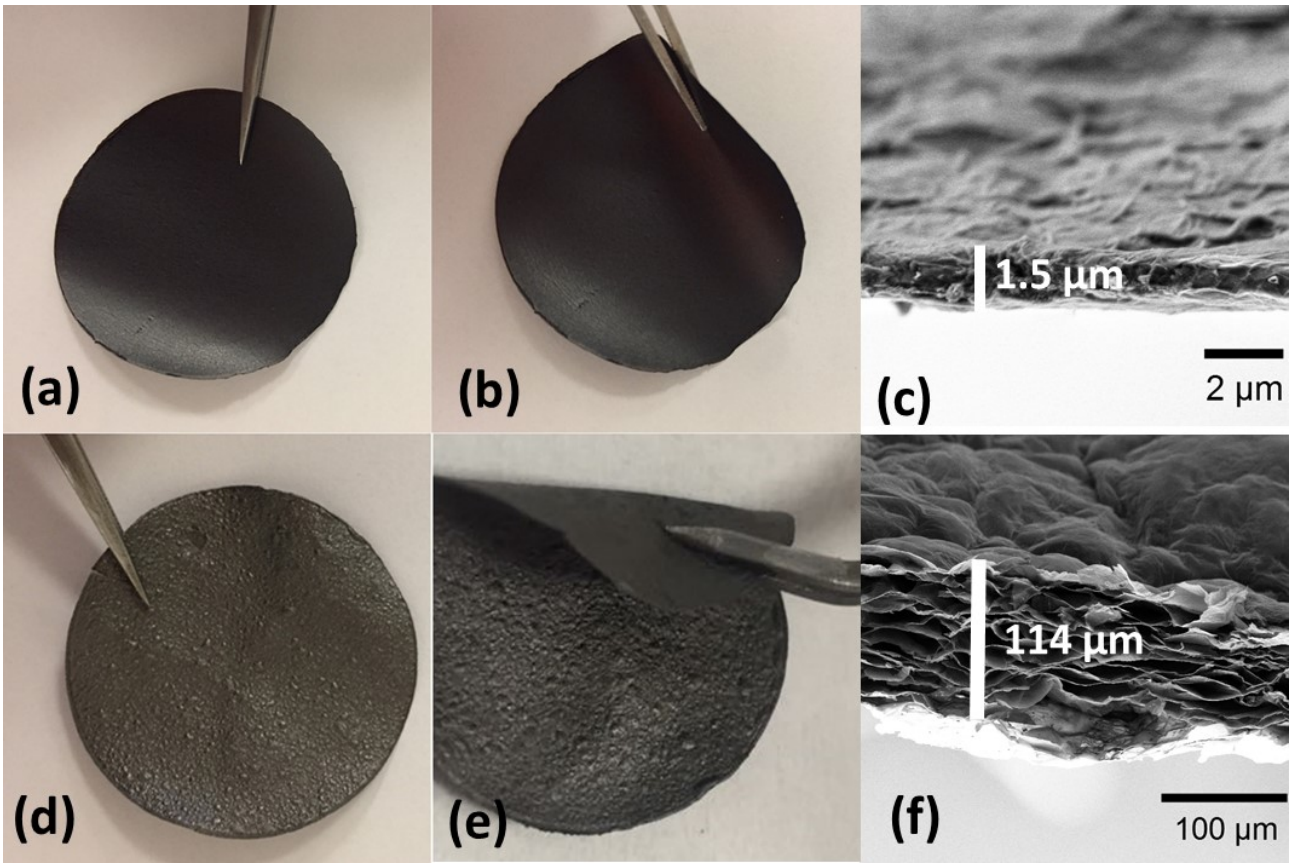

Figure 2-2: Digital images of self-standing (a,b) GO and (d,e) rGO papers. Cross-sectional FESEM images of (c) GO and (f) rGO papers.

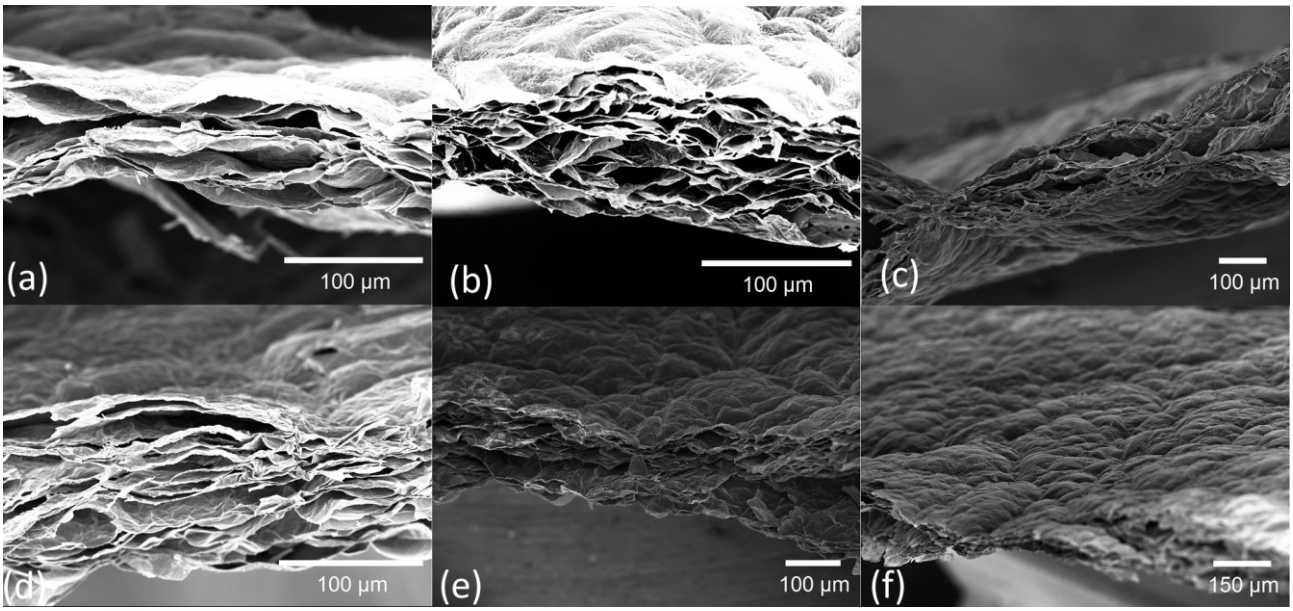

Figure 2-3: Cross-sectional FESEM images of rGO papers reduced via chemical reduction at different time intervals (a) 6h, (b) 10h, (c) 24h ; (d) thermally annealed after chemical reduction 6h+T, (e) 10h+ T, (f) 24h+T.

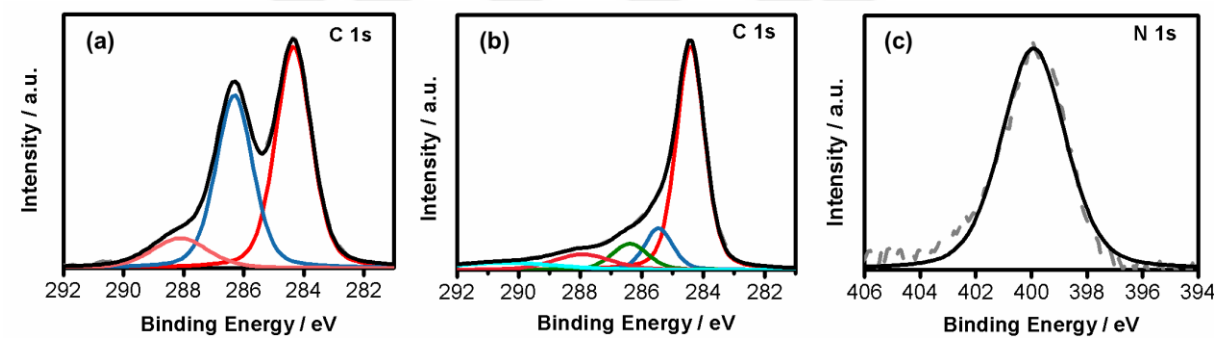

Figure 2-4: C1s spectra of (a) GO, (b) rGO, and (c) N1s spectrum of rGO.

XPS was utilized to evaluate the surface chemical structure of the GO and rGO papers. Figure 2-4a shows XPS C 1s spectrum of GO. The spectrum was deconvoluted into three peaks at 284.4, 286.3, and 288.1 eV, which are assigned to carbon-carbon (C-C/C=C/C-H) bonds, carbon singly bound to oxygen (hydroxyl and epoxide), and carbon doubly bound to oxygen (carbonyl and carboxyl), respectively [87]. The surface contains 73.6 % C and 27.4 % O, atomically. After reduction with hydrazine vapor for 10 hours, there was a significant decrease in the relative intensities of C-O and C=O peaks (normalized to C-C peak) compared to that of GO (Figure 2-4b). Additionally, two peaks appeared around 285.5 and 290.4 eV, which belong

to C-N bond and π-π* shake-up satellite, respectively [88]. A symmetric peak centered at 399.9 eV in the N 1s spectrum indicates formation of pyrazoline groups after treatment with hydrazine vapor [89]. Overall, the surface of rGO contains 82.8 % C, 12.4 % O, and 4.8 % N, which shows successful reduction of GO paper with hydrazine vapor along with nitrogen doping. The effect of different reduction methods on the surface chemistry was also evaluated by XPS analysis. Figure 2-5 and Figure 2-6 show deconvoluted C 1s and N 1s spectra of rGO papers reduced via chemical reduction and thermal annealing, respectively. C 1s spectrum of each sample was deconvoluted into five components. The corresponding peak intensities of functional groups normalized to C-C bond are given in Table 2-2. Thermal annealing after chemical reduction did not result in a significant decrease in the relative intensities of C-O, C=O, and C-N peaks. It is seen that C/(C+O) ratio (calculated from fitted C 1s and O 1s spectra of rGO papers) was slightly increased with thermal annealing, meaning that thermal annealing provides further reduction and the removal of residual oxygen-containing groups.

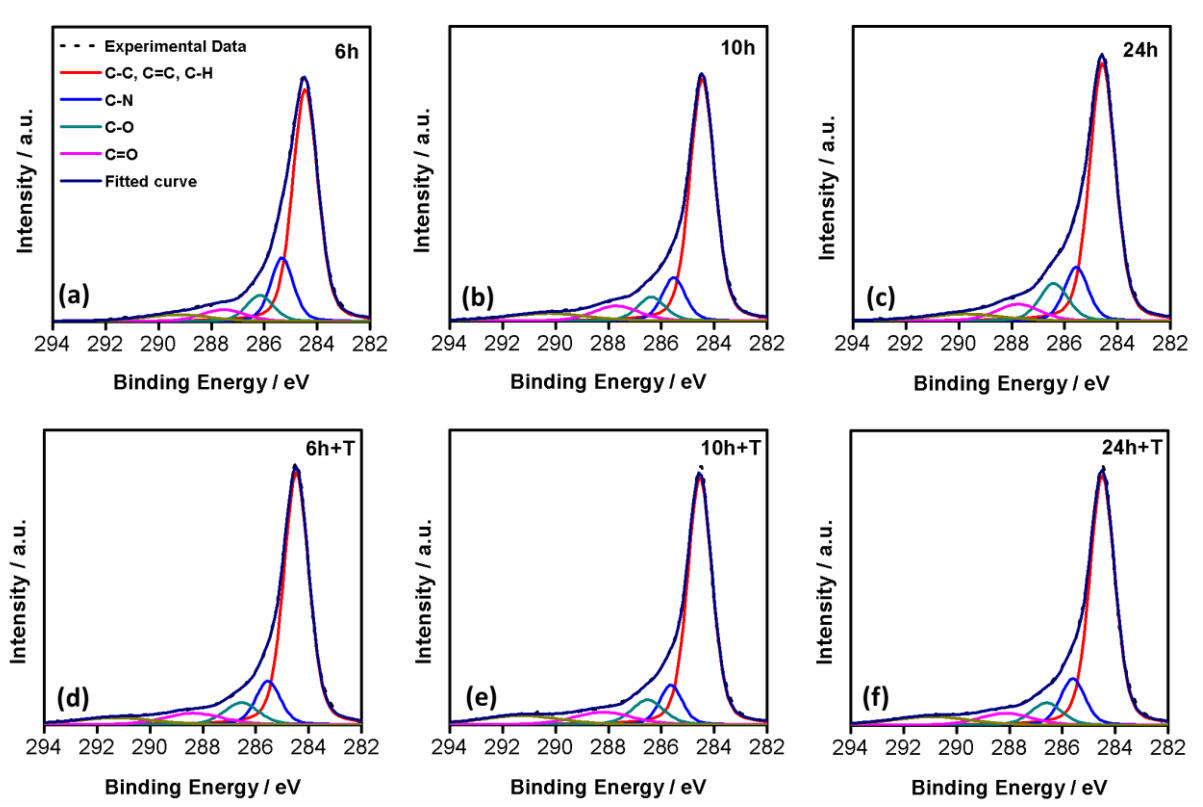

Figure 2-5: C1s XPS spectra of rGO films after treatment with hydrazine for 6h (a), 10h (b), 24h (c) 6h+T (d), 10h+T (e), 24h+T(f).

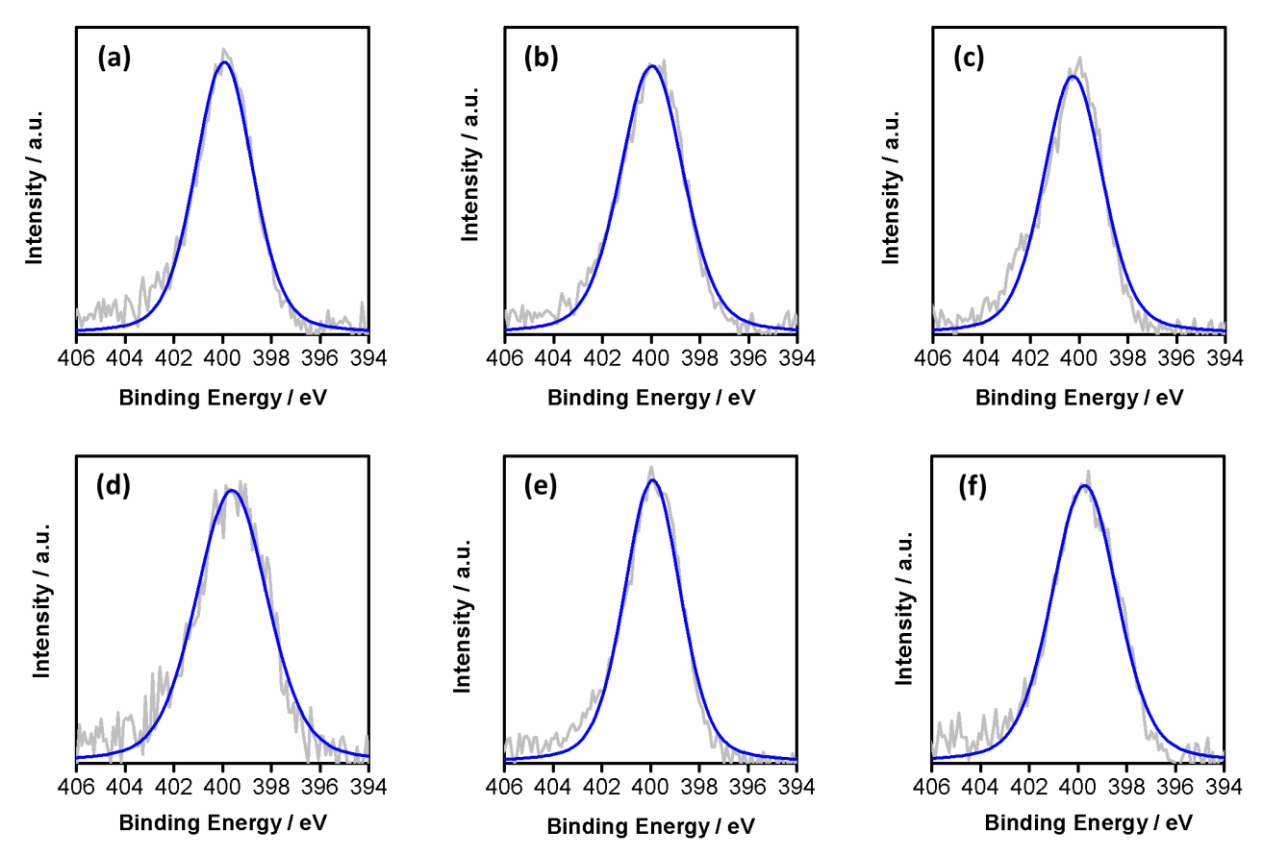

Figure 2-6: N1s spectra of XPS spectra of rGO films (a) 6h, (b) 10h, (c) 24 h, (d) 6h+T, (e) 10h+T, (f) 24h+T

Raman spectra of rGO papers were recorded in the range of 850-2000 cm^{-1} (Figure 2-7). Spectra are deconvoluted into three Pseudo-Voigt (around 1350, 1580, and 1610 cm^{-1}) and two Gaussian peaks (at around 1100 and 1500 cm^{-1}). The spectra of rGO papers display prominent peaks around 1350 cm^{-1} and 1585 cm^{-1} which are associated with D and G band of carbon materials [90]. The peak around 1100 cm^{-1} (D*) is associated with disordered graphitic lattice [91]. The peaks around 1350 and 1610 cm^{-1} are assigned to D and D' bands, respectively, which are both disorder-induced Raman modes. Thus, D and D' modes are forbidden in the perfect crystalline graphite [92]. Vollebregt et al. claimed that the intensity of D'' band decreases with the increase in crystallinity [93]. Finally, G band is in-plane vibrational mode of sp^2 carbon network.

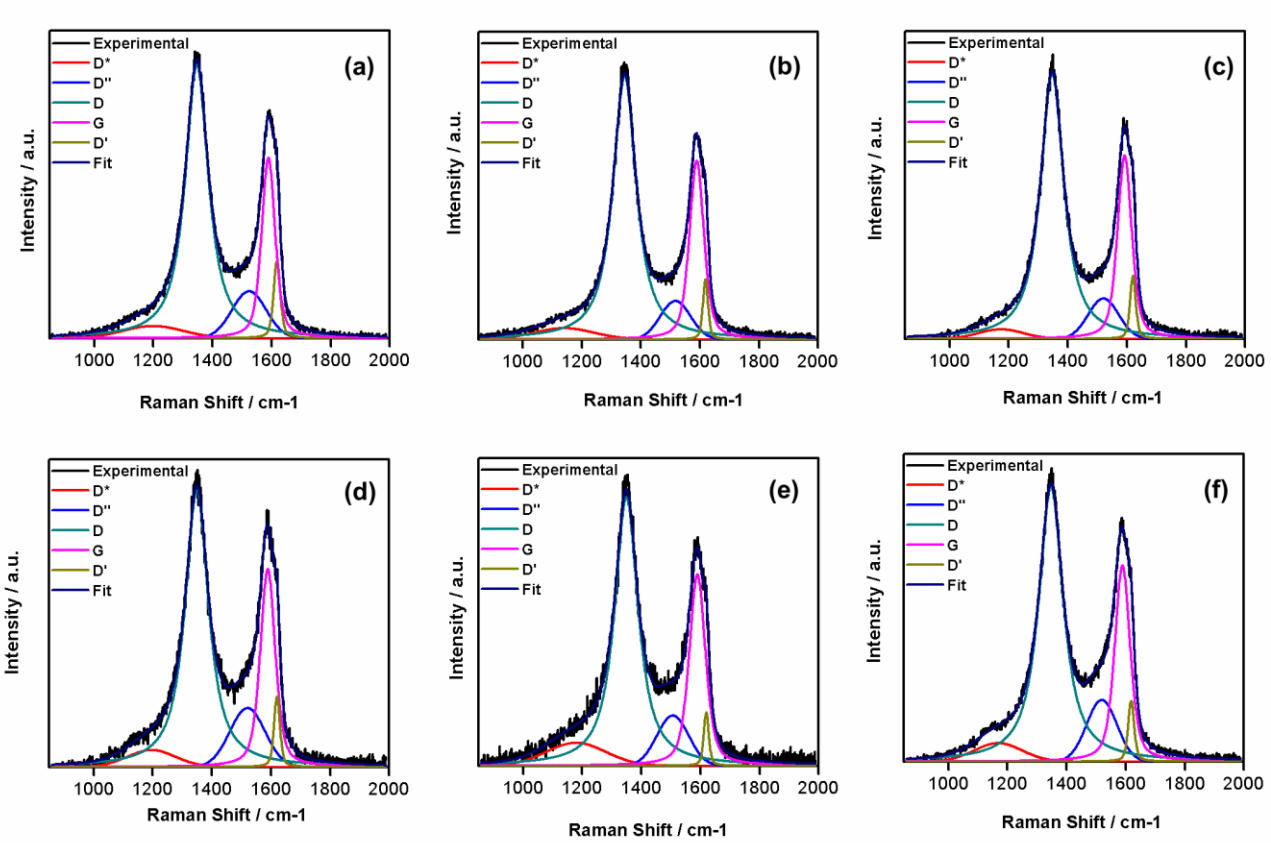

Figure 2-7: Fitted Raman spectra of GO papers reduced for (a) 6h , (b) 10h, (c) 24h, (d) 6h+T, (e) 10h+T, (f) 24h+T

Regarding the aforementioned information, I_D/I_G intensity ratio gives information about the degree of defects in the graphene network [91]. Increasing chemical reduction time from 6 hours to 10 hours results in decrease in I_D/I_G ratio in spectra (Table 2-1). However, after 10 hours, the ratio does not decrease significantly. $I_{D'}/I_G$ follows the same trend. This shows that annealing after chemical reduction results in removal of some defects in the graphene structure. Moreover, while I_{D*}/I_G ratio decreases with increasing chemical reduction time, this ratio increases with thermal annealing. Additionally, $I_{D''}/I_G$ also increased after thermal annealing of the samples. Both trends in I_{D*}/I_G and $I_{D''}/I_G$ revealed formation of more disordered structure with less crystallinity after thermal annealing. D and G band positions are also given in Table 2-1. Since the reduction results in red-shift in D and G band positions [94], the sample reduced via chemical reduction followed by thermal annealing for 10 h is the most reduced one according to Raman spectra.

Table 2-1. Peak intensities and peak positions calculated from Raman spectra of rGO papers

Sample	I_D/I_G	I_{D*}/I_G	$I_{D''}/I_G$	$I_{D'}/I_G$	D (cm^{-1})	G(cm^{-1})
6h	1.54	0.07	0.27	0.44	1347	1589
10h	1.48	0.06	0.23	0.37	1345	1589
24h	1.47	0.06	0.24	0.37	1347	1592
6h+T	1.40	0.09	0.31	0.35	1349	1589
10h+T	1.39	0.11	0.26	0.30	1350	1590
24h+T	1.41	0.10	0.31	0.31	1348	1589

Table 2-2. Relative intensities of functional groups in rGO papers normalized to C-C bond

Sample	**C-O**	**C=O**	**C-N**	**C/(C+O)**
6h	0.11	0.05	0.28	88.7
10h	0.10	0.06	0.18	89.4
24h	0.15	0.07	0.21	84.9
6h+T	0.09	0.05	0.17	89.2
10h+T	0.10	0.05	0.21	92.5
24h+T	0.09	0.05	0.19	91.8

2.3.2. Electrochemical Properties of Reduced Graphene Oxide Paper

First, effect of chemical reduction durations on the electrochemical properties was investigated. CV curves of rGO films reduced for different durations are given in Figure 2-8. While the CV curve of the film reduced for 10 h is quasirectangular, CV curves of the films reduced for 6 and 24 h are distorted and more polarized. Corresponding areal and specific capacitances calculated from the area under CV curves are given in

Table 2-3. While changing chemical reduction duration has slightly affected the total capacitance, thermal annealing after chemical reaction results in a dramatic decrease (around 10-fold). According to the study of Stankovich et al. [42] and the DFT calculations performed

by Kim et al. [43], chemical reduction with hydrazine results in the complete removal of epoxy groups, while other oxygen containing groups such as hydroxy and carboxyl are remained. These functional groups in GO structure contributes to the pseudocapacitive behavior in addition to double-layer capacitance of graphene and enhance the overall capacitance [95,96]. After thermal annealing, specific capacitances decreased dramatically, since thermal annealing removes the most of the residual oxygen-containing groups [36]. Among the thermally annealed papers, the one thermally annealed after chemical reduction for 24 h has the lowest capacitance and the reason could be that in cross-sectional FESEM images, 24h+T sample has the lowest thickness. Compact layers could lead to decrease in capacitance due to the lower surface area and the porosity. Additionally, Raman spectra show that thermal annealing decrease the amount of defect and defects contribute to overall capacitance [97].

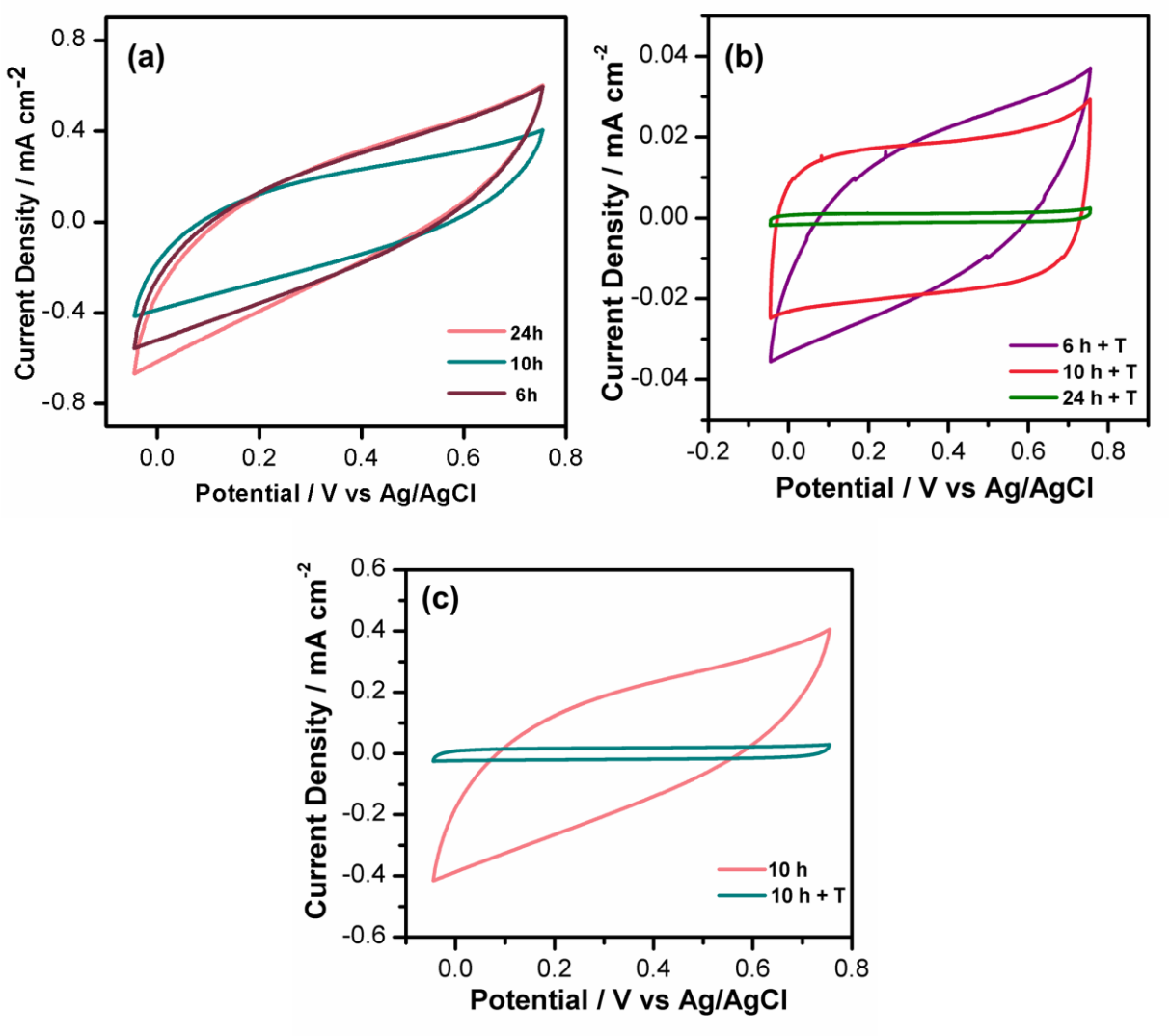

Figure 2-8: Cyclic voltammograms of (a) sample reduced chemically at different time intervals, (b) thermally annealed sample followed by the chemical reduction at different time intervals, (c) thermally annealed sample after the chemical reduction for 10 h GO papers at the scan rate of 20 mVs^{-1}.

Table 2-3. Areal and specific capacitances of rGO papers calculated from CV measurements at the scan rate of 20 $mV\ s^{-1}$.

Sample	Mass (mg)	Areal Capacitance ($mF\ cm^{-2}$)	Specific Capacitance ($F\ g^{-1}$)
6h rGO	3.73	9.53	5.11
10h rGO	3.52	7.28	4.13
24h rGO	3.51	9.87	5.63
6h+T rGO	2.81	0.75	0.54
10 h+T rGO	3.14	0.87	0.56
24 h+T rGO	2.95	0.05	0.03

2.3.3. Conclusion

In summary, graphene oxide solution was prepared via Hummers' method from graphite powder precursor. Self-standing GO papers were prepared via vacuum filtration and dried for 24 h at ambient atmosphere. XRD revealed that graphene oxide was synthesized successfully.

Effect of chemical reduction duration and thermal annealing on the morphology and electrochemical performances was evaluated. XPS results showed that reduction duration does not result in significant changes in C/(C+O). Also, Raman results show that the number of defects is decreased with thermal annealing. Chemically reduced GO papers with hydrazine vapor exhibited superior electrochemical performances compared to thermally annealed papers.

Chapter 3: Electrodeposition of Manganese Oxide onto Self-Standing Reduced Graphene Oxide Papers

The result presented in this chapter is published as a full article in Electrochimica Acta in 2019 [98].

3.1. Introduction

Due to depletion of fossil fuels and global warming, there is an increasing need for clean and renewable energy as well as efficient energy storage technologies [99]. Energy storage systems such as batteries and supercapacitors are required for balanced and continuous power supplies [48]. ECs have received great attention due to their high energy density and high charge-discharge efficiency [100]. Based on the energy storage mechanism, ECs are classified into two types: electrical double-layer capacitors (EDLCs) and pseudocapacitors. In EDLCs, electrostatic charge accumulation at the interface between the electrode and the electrolyte is utilized to store energy [101]. Carbonaceous materials including activated carbon, carbon nanotubes (CNT), graphite and graphene are used as electrode materials for EDLCs because they have relatively high surface area, (electro)chemical stability, and good electrical conductivity [102]. Conversely, fast and reversible redox reactions take place on the surface of electrodes in pseudocapacitors. Faradaic redox reactions occurring in pseudocapacitors result in greater energy density and higher specific capacitance (SC) than EDLCs [103]. Transition metal oxides, such as RuO_2 [104], V_2O_5 [105], MoO_3 [106], Co_3O_4 [107], MnO_2 [108], and TiO_2 [109] have been widely used as pseudocapacitive materials [110,111].

In recent years, flexible supercapacitors have gained importance because they can be utilized in portable electronics, wearable devices, implantable medical devices, and bendable displays [112]. Binder-free assembled free-standing electrodes with satisfactory electrochemical performance and large surface area are desirable as device components [113,114]. Graphene is a promising electrode material as a flexible supercapacitor owing to its excellent electrical

conductivity, large surface area, high mechanical strength, and good electrochemical stability [102]. Moreover, manganese oxides have been exploited as pseudocapacitors because of their environmental friendliness, low-cost, abundance, and high theoretical specific capacitance [115]. A variety of techniques including layer-by-layer assembly [116], chemical vapor deposition [117], electrophoresis [118], and electrodeposition [119] are used to produce manganese oxide thin films. Among these methods, electrodeposition allows production of thin and uniform films with various crystal structures and morphologies by tuning the pH, temperature, potential, and charge passed during electrodeposition [119].

Flexible papers composed of carbon derivatives (carbon fiber, carbon nanotube, graphene) are promising current collector materials compared to flat metal substrates. One obvious advantage is the dramatic decrease in mass per unit area (or volume) which has a direct influence on the energy density of the device. Additionally, the surface of carbon materials can be easily modified to create functional groups, which can act as binding/anchoring sites for the deposited metal oxides. Previously, it has been demonstrated that the electrochemical performance of manganese oxide can be enhanced when deposited on carbon-containing self-standing current collectors. In this regard, Wu *et al.* [120] reported anodic electrodeposition of MnO_2 on carbon fiber paper (CFP) and stainless steel (SS). The specific capacitance (SC) of needle-like MnO_2 nanofibers coated on CFP reached SC of 432 F g^{-1} at 5 A g^{-1}, which is higher than that of MnO_2 coated on SS (177 F g^{-1}). Moreover, Hu *et al.* [121] showed that MnO_2 nanostructures deposited on CNT-textile can achieve 10-times higher specific capacitance than that on Pt plate. The aforementioned and several other studies [113,122–125] utilized anodic electrodeposition to produce MnO_2 nanostructures on carbon substrates. Conversely, cathodic electrodeposition is utilized in this study to produce Hausmannite phase manganese oxides (Mn_3O_4) since the method does not cause oxidation and dissolution of the substrate during deposition, unlike the

anodic one. Additionally, cathodic current flow results in formation of porous structures since deposition occurs along with continuous hydrogen gas evolution on the working electrode [56]. In this chapter, one step cathodic electrodeposition of Mn_3O_4 onto self-standing reduced graphene oxide (rGO) paper is presented. Cathodic electrodeposition is carried out at ambient temperature and pressure from manganese nitrate solution. The structural properties of the thin deposits are investigated by Field-Emission Scanning Electron Microscopy (FESEM), Raman spectroscopy, and X-Ray Photoelectron Spectroscopy (XPS). Mn_3O_4 deposited on rGO papers are directly used as EC electrodes without additional metal current collectors. For the evaluation of electrochemical characteristics, cyclic voltammetry (CV), charge-discharge (CD), and electrochemical impedance spectroscopy measurements are conducted.

3.2. Materials and Methods

3.2.1. Materials

All chemicals are used without further purification. Graphite (natural, 99.9995%), $Mn(NO_3)_2$, $NaNO_3$ (99%), and Na_2SO_4 were obtained from Alfa Aesar. $KMnO_4$ and H_2O_2 (30%) were obtained from Merck Millipore. HCl (37%), H_2SO_4 (95-97%) and hydrazine monohydrate (98%) were obtained from Sigma Aldrich. Standard Calomel Electrode (SCE, in saturated KCl) was purchased from Radiometer Analytical. Filter papers (cellulose nitrate, 0.45 μm) were obtained from Sartorius Stedim Biolab. All solutions were prepared with doubly distilled water.

3.2.2. Synthesis of Graphene Oxide

Colloidal graphene oxide solution used in this chapter was synthesized as explained in Section 2.2.2.

3.2.3. Production of Self- Standing Reduced Graphene Oxide Papers

rGO papers used in this chapter were produced as explained in Section 2.2.2.1. The chemical reduction duration for all the rGO papers used in this chapter was 10 h.

3.2.4. Electrodeposition of Manganese Oxide Nanostructures

Electrodeposition was carried out with chronoamperometry at potentials ranging from -1.1 to -1.4 V vs. Ag/AgCl in a three-electrode electrochemical cell at room temperature. rGO paper, platinum sheet, and SCE were used as working, counter, and reference electrodes, respectively. The potentials in this study are reported vs. Ag/AgCl for ease of comparison. Deposition area was fixed to 1 cm^2. 25 mL freshly prepared aqueous solution of $Mn(NO_3)_2$ (50 mM) and $NaNO_3$ (50 mM) was used as the deposition bath. The electrodeposition process was performed with a potentiostat/galvanostat (Biologic VSP). After deposition, films were washed with water and left to dry at room temperature for 24 h. To calculate the deposited mass of manganese oxide, rGO papers were weighed before and after electrodeposition with Mettler Toledo XP6 microbalance (accuracy of 1 µg).

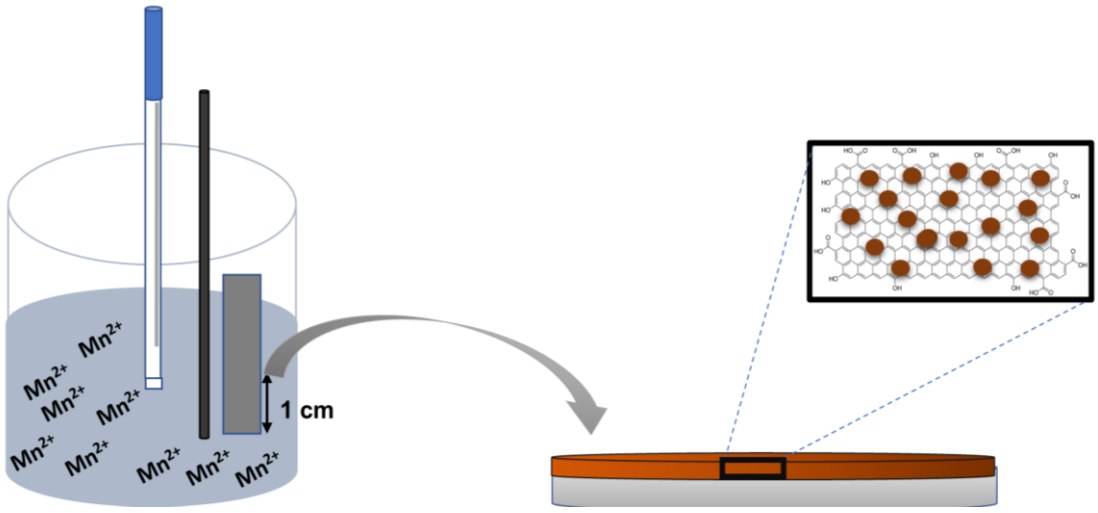

Figure 3-1: Schematic illustration of the cathodic electrodeposition of manganese oxide onto rGO paper.

3.2.5. Structural Characterization of Manganese Oxide deposited rGO paper

For the morphological analysis, FESEM (Zeiss Ultra Plus) was used. Crystal structure of deposited manganese oxide was evaluated by Raman Spectroscopy (Renishaw Invia) with 532 nm laser and power of laser was fixed to 0.6 mW. For each sample, three different measurements were done to ensure reproducibility. Surface chemical structure was analyzed

with XPS (Thermo K-Alpha) with Al Kα source. Fitting of the raw data was performed with Avantage software.

3.2.6. Electrochemical Characterization of Manganese Oxide deposited rGO paper

Electrochemical properties of Mn_3O_4 coated rGO papers (Mn_3O_4/rGO) were investigated by CV and galvanostatic CD in 0.5 M Na_2SO_4 electrolyte. Self-standing rGO paper coated with Mn_3O_4 was utilized as the working electrode without using any additional current collectors. Graphite rod and SCE were used as the counter and reference electrodes, respectively. CV measurements were performed between 0.0 V and 0.8 V (vs. Ag/AgCl) at scan rates from 1 to 100 mV s^{-1}. CD measurements were carried out at different current densities from 0.5 to 10 A g^{-1} over the potential window 0.0-0.8 V vs. Ag/AgCl. To evaluate the contribution of rGO paper to the overall capacitance, CV and CD measurements of bare rGO paper were also carried out within the same potential window. Impedance measurements were performed in the frequency range 500 kHz-100 mHz with a potential amplitude of 10 mV.

A symmetric cell was assembled with two identical Mn_3O_4/rGO papers for the calculation of energy and power density. Prior to the two-electrode measurements, the papers were immersed into the electrolyte solution (0.5 M Na_2SO_4) for 30 min. For the electrical contact, Au plates were placed at the edge of uncoated side of rGO papers. Energy density (E) and power density (P) values are calculated according to the following equations:

$$E = \frac{1}{2}\, C\, V^2$$

$$P = \frac{E}{\Delta t}$$

where C is the cell capacitance calculated from the discharge curves, V is the potential window of charge-discharge measurements, and Δt is the discharge time.

3.3. Results and Discussion

3.3.1. Structural Properties of Manganese Oxide deposited rGO paper

Figure 3-2 shows Raman spectra of deposited films in comparison with GO and rGO. In all the Raman spectra, the peaks around 1350 and 1590 cm^{-1} correspond to D and G bands of GO, respectively [126]. D band is related to structural defects since it is associated with breathing oscillation of six-membered carbon rings and this mode is forbidden in perfect crystals [90]. On the other hand, G band is the first-order scattering of E_{2g} phonons from sp^2 hybridized C-C bonds and it is associated with the graphitic carbon. With the reduction in hydrazine vapor, D and G bands of GO were red-shifted, (1350 to 1347 cm^{-1} and 1601 to 1587 cm^{-1} for D and G, respectively) and such a shift has been reported for chemically-reduced GO [38,42]. Deposition of manganese oxide film onto rGO paper results in the formation of a strong peak around 650 cm^{-1}. This peak is the A_{1g} vibration mode of Mn_3O_4. The presence of two smaller peaks in the region 300 - 360 cm^{-1} in all the spectra validates that the deposited manganese oxide is in Hausmannite phase [127]. In Raman spectra of all the deposited films, the positions of peaks belonging to rGO are similar indicating that the chemical structure of rGO was not affected by the cathodic electrodeposition.

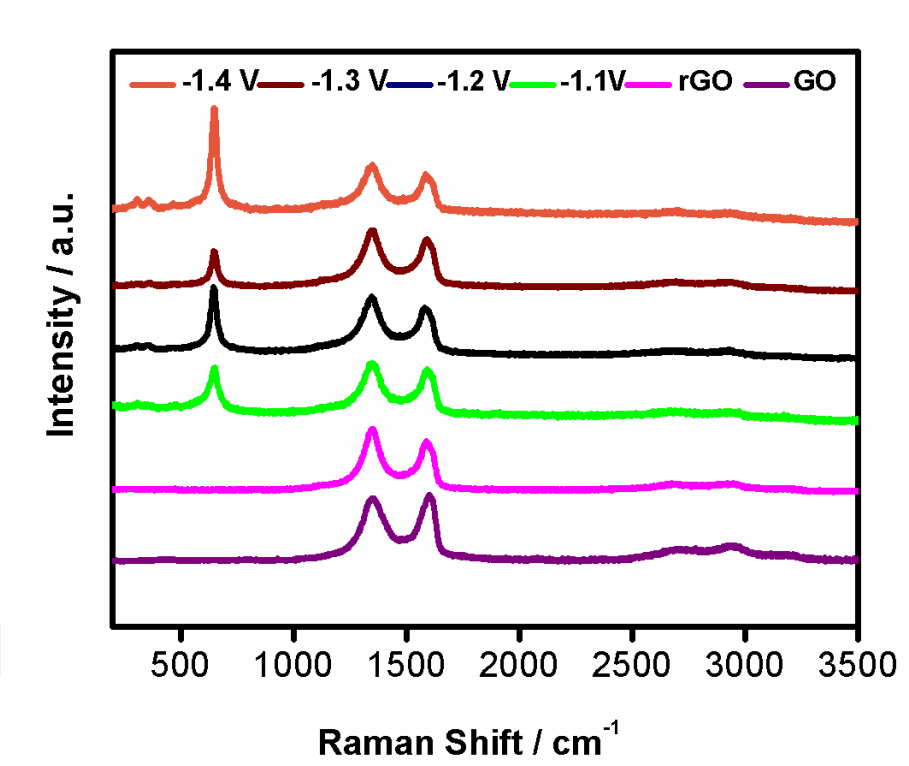

Figure 3-2: Raman spectra of GO, rGO, and Mn_3O_4/rGO deposited at different potentials

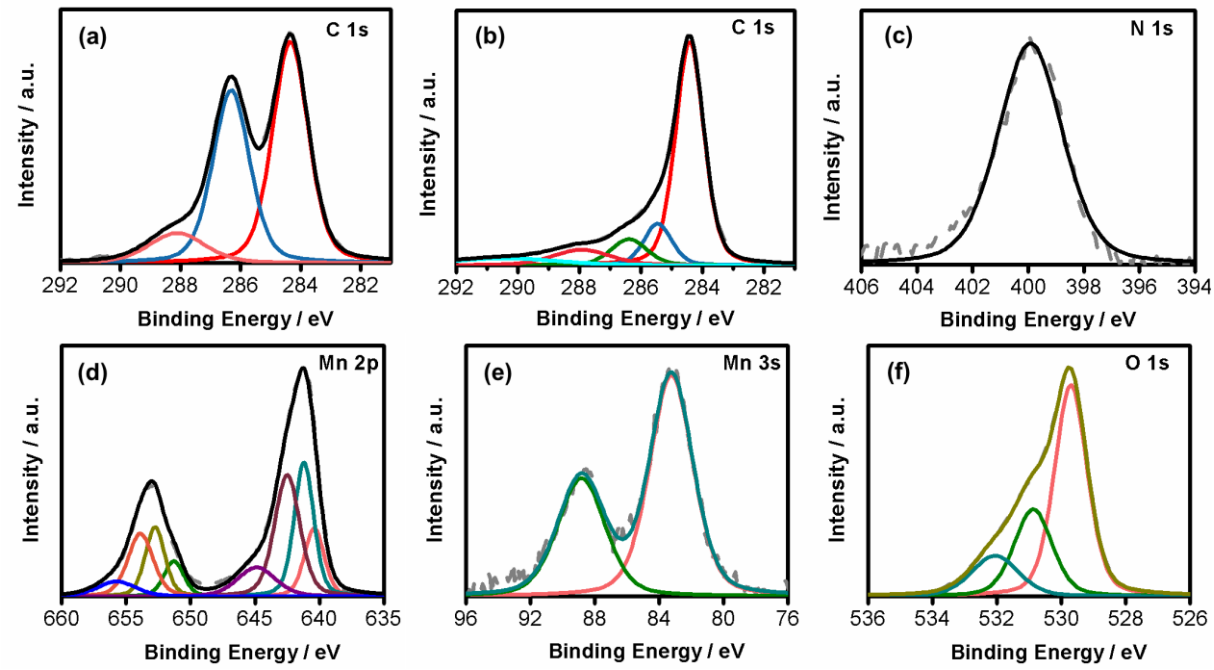

Figure 3-3: XPS C1s spectra of GO (a), rGO (b) ; N1s spectrum of rGO (c); Mn 2p (d), Mn 3s (e), and O 1s spectra of Mn3O4 film deposited at -1.1 V with fixed charge of 500 mC.

The chemical structures of the as-deposited MnO_x films were also investigated with XPS. Figure 3-3d shows Mn 2p spectrum of the sample deposited at -1.1 V. The peaks are broadened due to multiple splitting. $2p_{3/2}$ peak was deconvoluted into four peaks at 640.4 (Mn^{2+}), 641.2 (Mn^{3+}), 642.5 (Mn^{4+}), and 644.9 eV (shake-up for Mn^{2+}) [128]. Mn $2p_{3/2}$ and Mn $2p_{1/2}$ have average binding energies of 641.4 and 653.2 eV, respectively. These binding energies correspond to Mn_3O_4 phase [129]. Although Mn 2p spectra gives valuable information about the crystal structure, Mn 3s splitting is generally utilized to determine the phase of manganese oxides more accurately. Mn 3s spectrum of MnO_x/rGO film has two peaks centered at 83.3 and 88.9 eV, which are split by 5.6 eV (Figure 3-3e). According to the correlation reported by Toupin et al. [130], this energy difference corresponds to the oxidation state of 2.3, which validates the Hausmannite phase. Furthermore, O 1s spectrum has three peaks at 529.7, 530.9, and 532.0 eV, which are Mn-O-Mn, Mn-OH, and structural/adsorbed water, respectively (Figure 3-3f) [131]. Since Mn-O-Mn peak contribution is the highest (58.2 %), manganese is mainly present in the oxide form at the surface (Table 3-1).

Table 3-1. Binding Energy Values of Mn 2p, Mn 3s, and O 1s and the corresponding peak parameters calculated from fitted XPS spectra of Mn_3O_4 film deposited at -1.1 V

Peak	Peak Identity	Binding Energy / eV	Peak Separation / eV	Peak Area %
Mn 2p	$2p_{3/2}$	641.4	11.8	-
	$2p_{3/2}$	653.2		
Mn 3s	First Peak	83.3	5.6	-
	Second Peak	88.9		
O 1s	Mn-O-Mn	529.7	-	58.2
	Mn-OH	530.9		23.8
	H-O-H	532.0		18.0

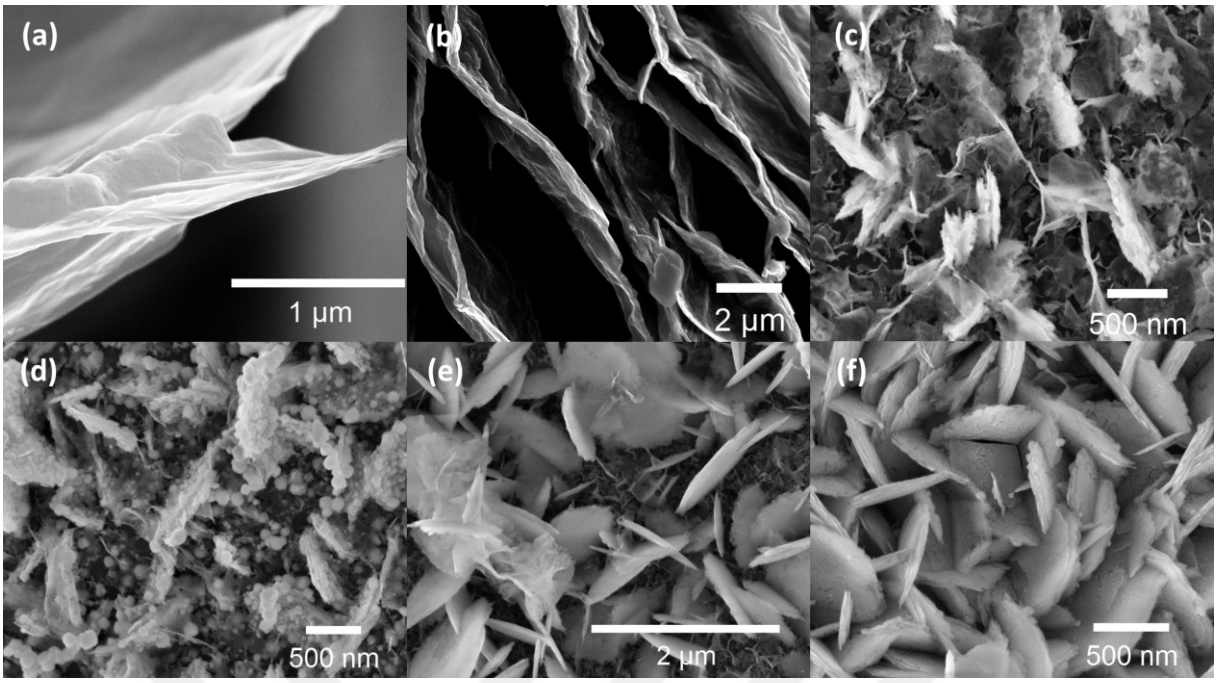

Figure 3-4: FESEM Images of rGO paper (a,b) and Mn3O4 films deposited at -1.1 V (c), -1.2 V (d), -1.3 V (e), and -1.4 V (f).

FESEM images of rGO paper and Mn_3O_4/rGO are shown in Figure 3-4. Reduction with hydrazine vapor results in the production of rGO foams as previously reported by Niu et al. [132]. In fact, it is also observed a similar foam like structure with expanded graphite multilayers in rGO paper reduced with hydrazine vapor (Figure 3-4a,b). When Mn_3O_4 is deposited at -1.1 V vs Ag/AgCl, nanoflowers covering overall surface of rGO were observed (Figure 3-4c). On the other hand, hexagonal plates decorated with nano-sized spherical particles were observed at -1.2 V (Figure 3-4d). At deposition potentials of -1.3 and -1.4 V, flakes with a well-defined hexagonal shape were obtained (Figure 3-4e, f). FESEM images revealed that the sample deposited at -1.4 V has more densely packed structures than others (Figure 3-4f).

While anodic electrodeposition results in direct oxidation of Mn^{2+} ions on the surface of the working electrode, cathodic electrodeposition proceeds with the generation of hydroxide ions by the reduction reactions of H_2O and NO_3^- according to the following reactions:

$$NO_3^- + H_2O + 2e^- \rightarrow NO_2^- + 2OH^-$$

$$2H_2O + 2e^- \rightarrow H_2 + 2OH^-$$

Formation of hydroxide ion as the product of the reactions above results in the precipitation of manganese hydroxide, $Mn(OH)_2$ [119]. Manganese hydroxide is not a stable product, so it is transformed into manganese oxide upon drying [133]. Evolution of the hydrogen gas during the electrodeposition prevents compact deposition of manganese oxide on the surface of the working electrode [56].

3.3.2. Electrochemical Properties of Manganese Oxide deposited rGO paper

Electrochemical performance of the films as EC electrodes was evaluated by CV measurements. SC values are calculated from the integration of CV curves according to the following equation:

$$SC\ (MnO_x) = \frac{Q_{total} - Q_{rGO}}{2 \times \Delta V \times m_{MnOx}}$$

where Q is the voltammetric charge, ΔV is the potential range of the measurement, and m is the mass of deposited manganese oxide. Because anodic and cathodic charges are not equal, the average is taken after calculating each side. Then, SC values are calculated based on MnO_x by subtracting the areal capacitance of rGO (at the same scan rate) from the total areal capacitance of the MnO_x/rGO followed by dividing into the mass of MnO_x.

To evaluate the effect of mass loading on the electrochemical performance, total charge was altered from 250 to 1000 mC during electrodeposition, resulting in the Mn_3O_4 loadings varying from 0.08 to 0.4 mg. As shown in Figure 3-5a, current response at the same scan rate (20 mV s^{-1}) is increasing with increase in the mass of Mn_3O_4. The corresponding SC values obtained from CV measurements at 20 mV s^{-1} for the samples with mass loadings of 0.08, 0.16, 0.3, and 0.4 mg are 125.8, 111.1, 102.5, and 66.3 F g^{-1}, respectively. The decrease in specific capacitance with increase in the amount of the active material is due to the limited charge transfer between the electrolyte and the bulk oxide material [134]. In thicker films, Mn_3O_4 structures deep in the film are not participating in redox reactions as effectively as the ones closer to the surface. Additionally, thicker films exhibit lower electrochemical performances because of low

electrical conductivity of manganese oxide. Although the highest SC is 125.8 F g^{-1} at 20 mV s^{-1} for the mass loading of 0.08 mg, incomplete surface coverage of Mn_3O_4 was observed in FESEM image of these films (not shown here). Thus, it is decided to proceed with the charge limit of 500 mC, which gave the second highest SC value along with uniform surface coverage. SC values of films deposited at different potentials of -1.1, -1.2, -1.3, and -1.4 V are calculated as 229.9, 216.9, 176.4, and 161.7 F g^{-1} at scan rate of 2 mV s^{-1}, respectively. It is apparent that the increase in the deposition potential results in decrease in the SC values of manganese oxide films. The sample deposited at -1.1 V yields the highest capacitance. As seen in Figure 3-5b, cyclic voltammograms of the film deposited at -1.1 V possess redox peaks of manganese oxide along with the distorted rectangular background indicating that both faradaic redox reactions and double-layer capacitive effects occur simultaneously [135,136]. Table 3-2 shows the corresponding SC values obtained from the voltammograms shown in Figure 3-5b SC values are increasing with decreasing scan rate from 100 to 1 mV s^{-1}. This is probably due to relatively slow diffusion of Na^+ ions into the manganese oxide lattice compared to scan rate. Lower scan rates provide more efficient insertion/deinsertion process which enhance the capacitance values [137,138]. Since cyclic stability of an EC electrode is an important criterion, the electrochemical stability of the films was evaluated by performing CV at 100 mV s^{-1} for 10000 cycles. Figure 3-5c represents the relative capacitance as a function of cycle number. The SC values increased drastically during the first 2500 cycles. In fact, 158 % capacitance increase was observed at 2500^{th} cycle when compared to the initial one reaching the maximum value throughout the measurement. When this maximum point is taken as the reference (2500^{th} cycle), 97 % capacitance retention was obtained at 10000 cycles. Figure 3-5d presents the Nyquist diagram of Mn_3O_4/rGO film. The diagram consists of a distorted semi-circle accompanied with a straight line. The equivalent circuit used to fit the experimental data is given in the inset. L represents self-inductance of the electrical connections, R_s is the solution resistance, Q_1 is the

constant phase element for the double-layer capacitance, R_{ct} is the charge-transfer resistance, W is the finite length Warburg element for the diffusion, and Q_2 is the constant phase element for pseudocapacitance [56]. The solution resistance calculated from fitting the equivalent circuit is 21.4 Ω which is higher than MnO_x deposited on metallic current collectors due to the resistance of self-standing rGO current collector. The charge transfer resistance (R_{ct}), on the other hand, is calculated as 10.0 Ω.

Table 3-2: SC values of MnO_X at different scan rates in CV and current densities in CD. The sample was deposited at -1.1 V with a fixed charge of 500 mC. The measurements were performed after 1000 cycles of CV at 100 mV s^{-1}.

Scan Rate / mV s^{-1}	**Specific Capacitance / F g^{-1}**	**Current Density / A g^{-1}**	**Average SC / F g^{-1}**
1	307.8	0.5	546.4
2	229.9	1	247.2
5	164.9	1.5	203.9
10	133.1	2	177.7
20	111.1	2.5	160.0
50	87.8	3.75	129.5
75	78.1	5	111.0
100	70.6	10	72.4

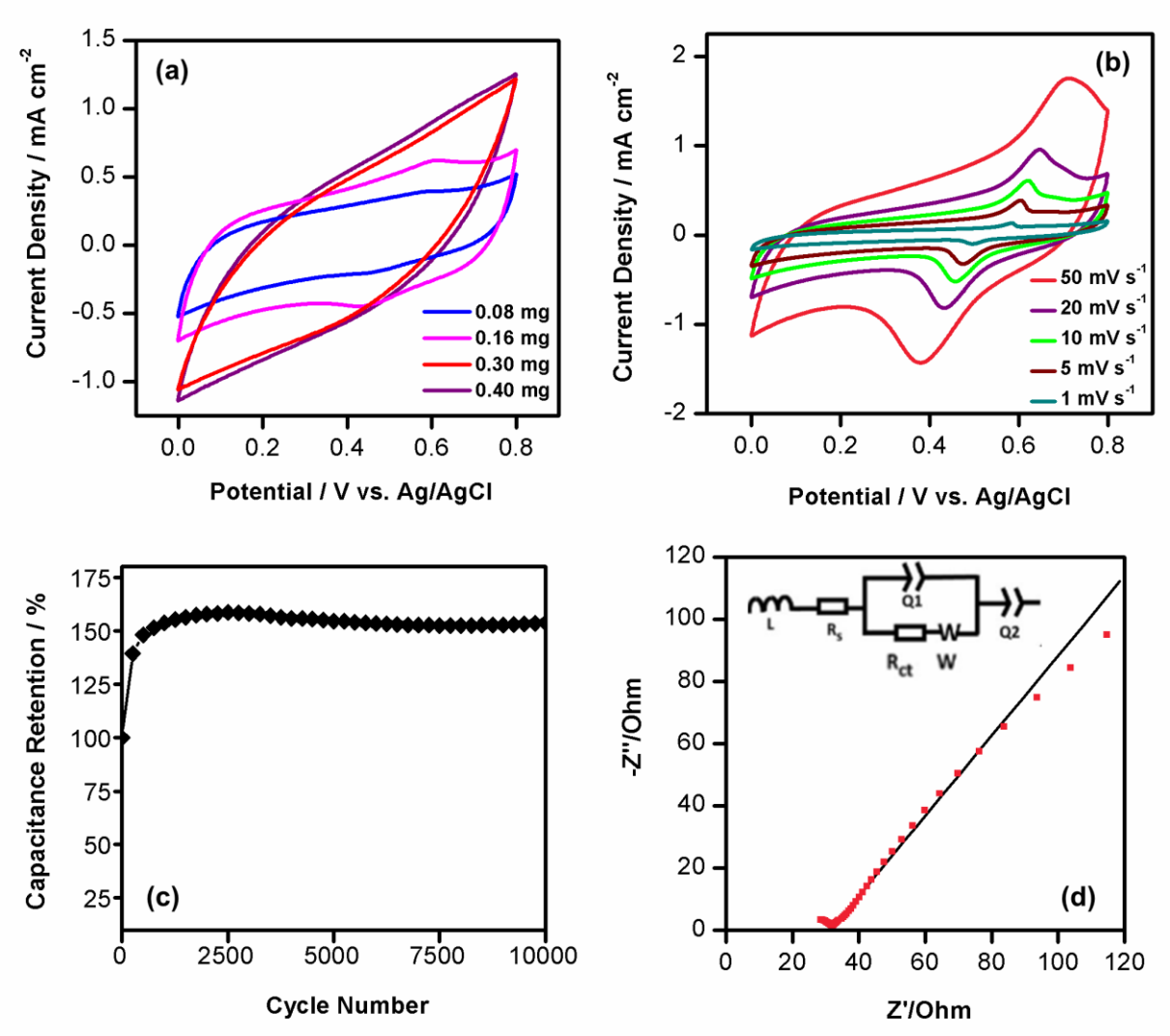

Figure 3-5: Cyclic voltammograms of Mn_3O_4/rGO with different mass loads at 20 mV s-1 (a); Cyclic voltammograms of Mn_3O_4/rGO deposited at -1.1 V with a fixed charge of 500 mC at different scan rates (b); Capacitance retention of the film as a function of cycle number (c); Nyquist diagram of Mn_3O_4/rGO along with the equivalent circuit to fit the experimental data (solid line represents the fitted curve).

Galvanostatic CD test was also carried out at different current densities over the potential window 0.0 - 0.8 V vs Ag/AgCl (Figure 3-6a). Figure 3-6b shows 10 representative CD cycles of the sample deposited at -1.1 V. Almost linear CD curves with small IR drops were observed, which verifies the good capacitive behavior of the composite. Shorter charge and discharge times were observed at high current densities and the highest SC was obtained at 0.5 A g^{-1}. Observation of lower SC values at higher current densities is analogous to the observation of lower SC at higher scan rates in CV. Average SC values are calculated according to the following equation and the corresponding values are tabulated in Table 3-2:

$$SC = \frac{(I_{total} \times \Delta t_{total}) - (I_{rGO} \times \Delta t_{rGO})}{m_{MnOx} \times \Delta V}$$

where I_{total} and I_{rGO} is the charge or discharge current densities of the Mn_3O_4/rGO and the bare rGO paper; Δt_{total} and Δt_{rGO} are the charge or discharge time of the rGO paper; m_{MnOx} is the mass of the active material, and ΔV is the potential range. The SC values at different current densities are summarized in Table 3-2. To calculate the average SC value of the film, charge and discharge capacitances were calculated separately and the average was taken to report average SC values. For the calculation of cell capacitance (based on MnO_x) of the symmetric device, similar route is followed with the 3-electrode measurement. A symmetric rGO//rGO cell is assembled separately, and the discharge time of this cell is subtracted from that of Mn_3O_4/rGO//Mn_3O_4/rGO to obtain the cell capacitance based on MnO_x. Galvanostatic charge-discharge curves of the symmetric device is shown in Figure 3-6c for different current densities. Similar to the three-electrode measurement, small IR drops are obtained with all the current densities applied. Ragone plot derived from the charge-discharge measurements of the symmetric cell is given in Figure 3-6d. The highest energy density is 6.9 W h kg^{-1} at 143 W kg^{-1} (0.5 A g^{-1}) and the lowest is 0.013 W h kg^{-1} at 2250 W kg^{-1} (10 A g^{-1}).

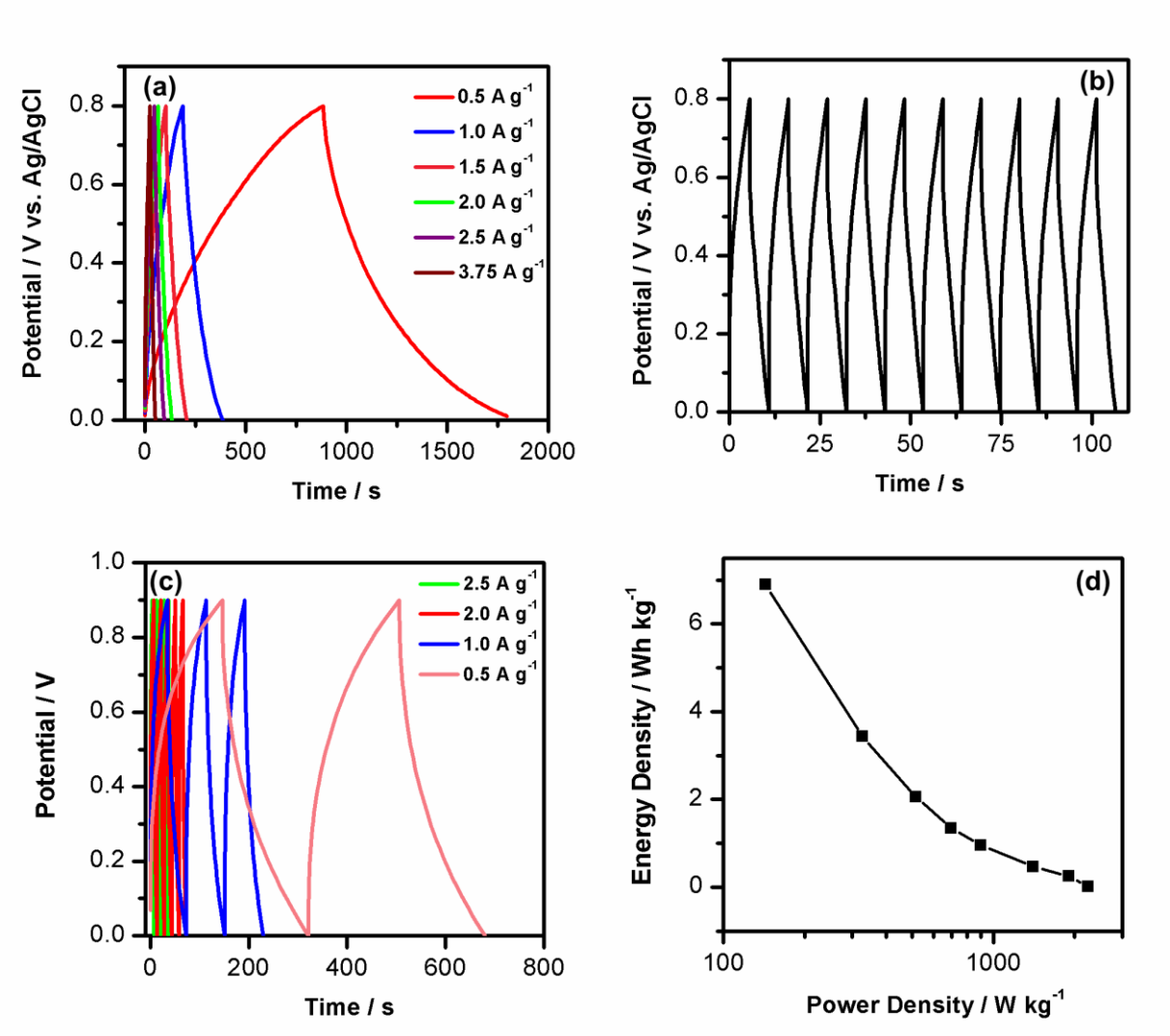

Figure 3-6: CD curves of MnOx at different current densities (a); Successive 10 CD curves at 10 A g^{-1} (b). The sample was deposited at -1.1 V with a fixed charge of 500 mC. The measurements were performed after 1000 cycles of CV at 100 mV s-1. CD curves of MnOx/ rGO//MnO_x/rGO symmetric cell at different current densities (c); Ragone plot for MnO_x/rGO//MnO_x/rGO symmetric cell.

Electrochemical tests were resulted in structural changes within the films to some extent. We have investigated the structural and chemical changes in the films during and after electrochemical tests. The obvious observation is the change in the physical look of films.

The color of deposited manganese oxide films was initially light brown, but the color turned to gray after CV measurements (Figure 3-7a). The detailed investigation of the structure of films after 10000 cycles revealed that needle-like particles are distributed in a continuous phase of manganese oxide structure as seen in the FESEM images of a film in Figure 3-7a and Figure

3-7b shows the Raman spectrum of the film after 10000 cycles of CV measurement, which consists of two peaks around 500 and 560 cm^{-1} corresponding to Birnessite (MnO_2) phase of manganese oxide [139]. The peak positions of rGO did not change during the CV measurement indicating that the surface of underlying rGO paper was unaffected by the deposition process and acted purely as a current collector.

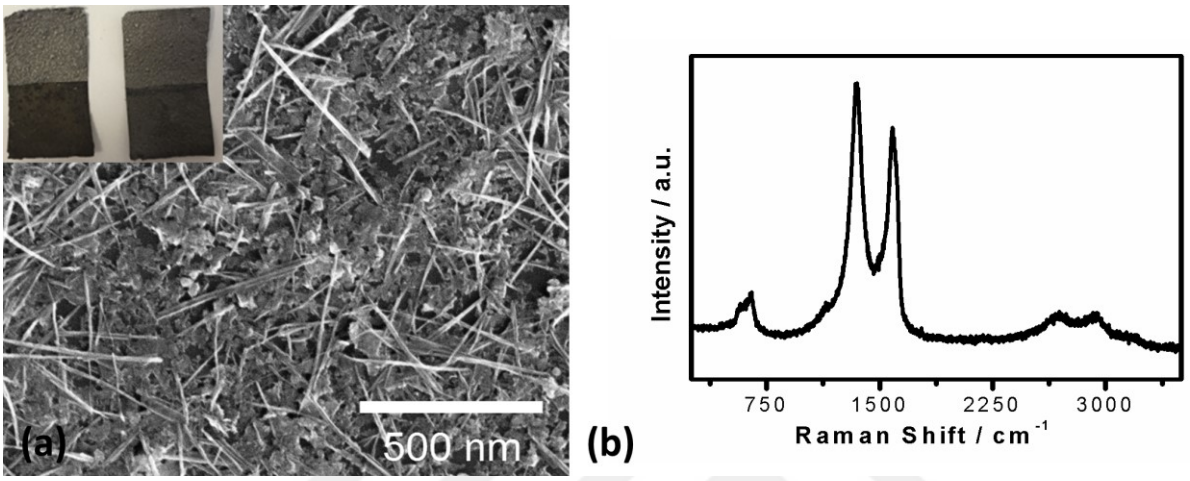

Figure 3-7: FESEM Image (inset shows digital images of the films before (left) and after CV (right) (a) and Raman spectrum of MnO_x/rGO film after 10000 cycles of CV (b). The sample was deposited at -1.1 V with a fixed charge of 500 mC.

The evolution of surface chemical structure of MnOx/rGO film was also investigated with XPS. Figure 3-8 shows Mn 2p spectrum of the film after cycling for 10000 cycles. The binding energy values of 2p3/2 and 2p1/2 were shifted to higher values, indicating an increase in the oxidation state (

Table 3-3). Additionally, the contribution of Mn^{2+} to the overall 2p3/2 peak lowered, while that of Mn^{4+} raised (Figure 3-8a). Splitting in the Mn 3s peak decreased after the stability test (Figure 3-8b and

Table 3-3). In fact, the difference of 5.1 eV corresponds to average Mn oxidation state of 3.2, which is almost 1.5 times higher than the original value. Thus, a mixed-valent MnO_x was formed during the potential cycling in agreement with the Raman result.

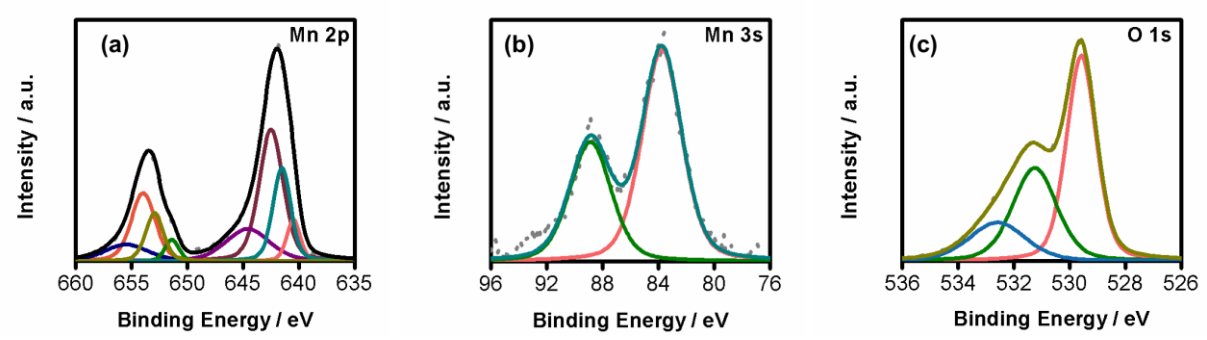

Figure 3-8: XPS Mn 2p (a), Mn 3s (b), and O 1s (c) spectra of MnOx film after 10000 cycles of CV. The sample was deposited at -1.1 V prior to CV.

Table 3-3. Binding energy values of Mn 2p, Mn 3s, and O 1s and the corresponding peak parameters calculated from fitted XPS spectra of MnO_x/rGO after 10000 cycles of CV.

Peak	Peak Identity	Binding Energy / eV	Peak Separation / eV	Peak Area %
Mn 2p	$2p_{3/2}$	642.0	-	-
	$2p_{3/2}$	653.6		
Mn 3s	First Peak	83.8	5.1	-
	Second Peak	88.9		
O 1s	Mn-O-Mn	529.6	-	49.5
	Mn-OH	531.2		33.1
	H-O-H	532.6		17.4

There are several reports regarding the electrodeposition of Mn_3O_4 on different substrates. For instance, Nagarajan *et al.* [140] performed cathodic electrodeposition of Mn_3O_4 on Ni foil. The film was annealed at 300 °C and the SC of the film was 445 F g^{-1} at 0.5 mA cm^{-2}. However, the film maintained 80% of its initial capacitance after 1000 cycles of CV at 50 mV s^{-1}. In 2015, Yang *et al.* [141] reported anodic electrodeposition of Mn_3O_4 on carbon fiber paper at 70 °C followed by annealing at 400 °C for 3 h. Resulting film had a SC of 230 F g^{-1} at 0.5 A g^{-1}. Moreover, our group reported electrochemical-hydrothermal synthesis of Mn_3O_4 films on Ni mesh. Produced films exhibited SC of 518.8 F g^{-1} at 0.1 mA cm^{-2} [56]. Similar to this study,

the last two reports also mention conversion of Mn_3O_4 to MnO_2 upon CV measurements. Nevertheless, our electrodes outperformed the above-mentioned films even though the films are synthesized at ambient temperature and does not require any annealing steps. Moreover, the performance of our converted- mixed-valent MnO_x electrodes are also better or comparable to MnO_2 deposited on carbon current collectors (see Table 3-4). Note that the composites of manganese oxides with graphene (oxide) are not included in the table since this material is also not a composite of manganese oxide and graphene. The promising performance of the reported material may be resulting from the formation of nanoneedle structures, which generally exhibit superior performances[125]. Also, mixed-valent phases of transition metal oxides exhibit excellent electrochemical performance [142].

Table 3-4. Summary of electrochemical performance of manganese oxide electrodes with carbon-containing current collectors.

Material	**Electrolyte**	**3-Electrode Performance***	**Capacitance retention**	**Reference**
MnO_2 on CNT paper	0.1 M Na_2SO_4	516.2 F g^{-1} (77 mA g^{-1}) 185 F g^{-1} (5 mV s^{-1}, MnO_2 loading: 0.8 mg cm^{-2})	88% after 3000 cycles	[122]
MnO_2 on CNT-textile	0.5 M Na_2SO_4	410 F g^{-1} (5 mV s^{-1}, MnO_2 loading: 0.06 mg cm^{-2})	60% after 10000 cycles	[121]
MnO_2 on CFP	1 M Na_2SO_4	274.1 F g-1 (0.1 A g^{-1})	95% after 5000 cycles	[143]
MnO_2 on nickel foam derived graphene	0.5 M Na_2SO_4	465 F g^{-1} (2 mV s^{-1})	82% after 5000 cycles	[113]
MnO_2 on CFP**	0.5 M Na_2SO_4	178 F g^{-1} (0.1 A g^{-1})	87.5 % after 2000 cycles	[144]
MnO_2 nanorods on CFP	0.5 M Na_2SO_4	362.5 F g^{-1} (0.5 A g^{-1})	96.5 % after 5000 cycles	[125]
MnO_2 on carbon nanofiber network	1.0 M Na_2SO_4	227 F g^{-1} (0.5 A g^{-1})	80% after 2000 cycles	[124]

* Reported values are based on the mass of active material (MnO_x) as calculated in this study.

** The composite MnO_2/rGO on CFP reported in the study is not included for reliable comparison.

3.4. Conclusions

In this chapter, Hausmannite phase of manganese oxide was coated onto rGO paper by one step electrodeposition route to produce electrode materials for electrochemical capacitors. Change in the morphology of films and electrochemical performance with the change of deposition potential were investigated in detail. Mn_3O_4 film coated at -1.1 V and room temperature exhibited the highest electrochemical performance and excellent cyclic stability in 0.5 M Na_2SO_4 electrolyte. During CV measurement, increase in capacitance value was observed which resulted from the phase transformation from Mn_3O_4 (nanoflowers) to mixed-valent MnO_x (nanoneedles).

Chapter 4: Self-Standing Reduced Graphene Oxide Papers Decorated with Superparamagnetic Iron Oxide Nanoparticles

This chapter includes a collaborative work between research groups of Assoc.Prof. Uğur Ünal and Assoc.Prof. Funda Yağcı Acar of Chemistry Department, Koç University.

4.1. Introduction

Graphene-based materials are promising candidates for flexible electrochemical capacitors due to their high electrical conductivity, high mechanical strength, superior theoretical surface area [1]. However, the main drawback of graphene-based materials is their low energy density because of their charge storage mechanism is mainly electrostatic. There has been numerous efforts to improve electrochemical performances of graphene-based electrodes [48,145,146]. General requirements for supercapacitors are long cycle life, quick charge discharge ability, high capacitance, and high energy density [147]. There are two approaches for increasing the energy density of ECs. The amount of stored energy can be enhanced either by increasing the working potential range or developing new electrode materials with high capacitances [148]. As the stored energy is directly proportional to the square of potential window, the magnitude of the working potential range of a supercapacitor leads to enhanced energy density. However, in aqueous electrolytes, water can be easily electrolyzed due to the thermodynamic potential window of water (1.23 V) [149]. Numerous efforts have been made to extend the operating voltage of supercapacitors in aqueous electrolytes. For instance, Jafta *et al.* reported manganese oxide/GO composites for high-energy asymmetric ECs with a working potential window of 2 V [150]. RuO_2/graphene nanocomposite asymmetric supercapacitor with an operation potential window of 1.8 V and an energy density of 55.3 Wh kg^{-1} was reported by Hwang *et al.* [151]. Furthermore, developing composite EC electrodes combining the EDLC mechanism of carbonaceous materials and pseudocapacitive mechanism of metal oxides can enhance the total capacitance of the system. Pseudocapacitive materials contribute to the system with high

specific capacitance, which results in high energy density. However, they suffer from low power density due to the limited rate of faradaic reactions [152]. In this regard, Fe_3O_4 is one of the most promising pseudocapacitive materials owing to its high theoretical capacitance, abundance, and low environmental impact. However, iron oxides acquire poor capacitance retention and have low electrical conductivity. Incorporating Fe_3O_4 with carbon-based materials such as carbon nanotubes, active carbon, and graphene will enhance the electrical conductivity via providing electron transportation channel. Additionally, the carbon skeleton will act as a support for Fe_3O_4 to prevent agglomeration, providing sufficient utilization of Fe_3O_4 in faradaic reactions [152,153]. Among these conductive supports, graphene is promising because of its high surface area, high electrical conductivity, and the ease of mass production. Also, the synergistic effect between Fe_3O_4 and graphene is beneficial for high electrochemical performances [154].

In the literature, there are several reports that focused on Fe_3O_4/ graphene composites as electrodes for electrochemical capacitors. In 2014, Liu and Sun reported Fe_3O_4/graphene composite paper as a flexible electrode with a specific capacitance of 368 F g^{-1} at 1 A g^{-1} along with 64.8% cyclic stability [155]. Wang *et al.* [156] studied the growth of Fe_3O_4 nanoparticles on graphene. They prepared Fe_3O_4/graphene composite with a specific capacitance of 220 F g^{-1} at a current density of 0.5 A g^{-1}. Furthermore, Li *et al.* presented dispersed Fe_3O_4 nanoparticles on reduced graphene with a specific capacitance of 241 F g^{-1} at 1 A g^{-1} and 79% cyclic stability at 1000 cycles [157]. In 2016, Das *et al.* [158] reported facile synthesis of Fe_3O_4 decorated rGO with a specific capacitance of 315 C g^{-1} at 5 A g^{-1} and 95% capacitance retention at 2000 cycles. In this chapter, preparation of Fe_3O_4 nanoparticles decorated self-standing rGO papers using electrostatic interaction between superparamagnetic iron oxide nanoparticles (SPION) and GO is presented. Composite papers are produced by simple vacuum-assisted filtration of colloidal

GO and APTMS coated SPION. To investigate the structural properties, XPS and FESEM are used. For electrochemical characterization, CV and GCD measurements are conducted.

4.2. Methods and Materials

4.2.1. Materials

All chemicals were used without further purification. Graphite (natural, 99.9995%), $NaNO_3$ (99%), and Na_2SO_4 were obtained from Alfa Aesar. $KMnO_4$, H_2O_2 (30%), $FeCl_2$. $4H_2O$, and $FeCl_3.6H_2O$ were obtained from Merck Millipore. Ammonium hydroxide, H_2SO_4 (95-97%), HCl (37%), and hydrazine monohydrate (98%) were obtained from Sigma Aldrich. 3-aminopropyl (trimethoxysilane) and Amicon filters (PES, 10K) are obtained from Galest (Germany) and Sartorius AG (Germany), respectively. Standard Calomel Electrode (SCE, in saturated KCl) was purchased from Radiometer Analytical SAS. Filter papers (cellulose nitrate, 0.45 μm) were obtained from Sartorius Stedim Biolab. All solutions were prepared with doubly distilled water.

4.2.2. Synthesis of Graphene Oxide

Colloidal graphene oxide solution used in this chapter was synthesized as explained in Section

4.2.3. Synthesis of (3-Aminopropyl) trimethylsilane (APTMS) Coated SPION

The synthesis and characterization of APTMS coated SPION was conducted in the Polymers and Nanomaterials Research Laboratory of Assoc. Prof. Funda Yağcı Acar at Koç University. APTMS coated SPION was prepared via coprecipitation of $FeCl_3.6H_2O$ and $FeCl_2.4H_2O$ salts under alkaline conditions with the salinization process of APTMS on nanoparticles. First, ferric and ferrous salts were mixed under argon atmosphere. During mixing, degassed APTMS and NH_4OH were injected to the reaction. The reaction was performed at 80 C for 1 h and the molar ratio between precursors was $[Fe^{2+}+Fe^{3+}]$: [APTMS]:[OH]= 1:0.8:15. The mixture was allowed to cool down while standing on 0.3 T magnet and mixed overnight to precipitate coalesced

particles. After magnetic precipitation was completed, the colloidal suspension was collected and purified via ultracentrifugal filtration (Amicon PES filter, 10K).

4.2.4. Preparation of Iron Oxide Nanoparticles Decorated Reduced Graphene Oxide Paper

To prepare iron oxide/reduced graphene oxide composites, two different methods were used. First, different volumes (25.0, 50.0, or 100.0 ul) of colloidal SPION solution with a concentration of 80.5 g/L was added to 10 mL of 3 g/L GO solution (10 mL), and the solution was stirred for 10 minutes. This mixture was directly filtered through filter paper. In the second method, SPION solution was added after the filtration of GO solution.10 mL of 3 g/L GO solution was filtered followed by the addition of 2 mL SPION solution with different concentrations. The addition of SPION was performed while the GO paper was still wet. Self-standing composite papers were reduced via hydrazine vapor reduction at 90 °C for 10 hours. The samples prepared via the first and the second technique are named thereafter “mixing” and “layer”, respectively.

4.2.5. Structural Characterization

For the morphological analysis, FESEM (Zeiss Ultra Plus) was used. XPS (Thermo K-Alpha) with Al Kα source was used to evaluate the surface chemical structure.

4.2.6. Electrochemical Characterization

Electrochemical properties of SPION/rGO papers were investigated by CV and galvanostatic CD in 0.5 M Na_2SO_4 electrolyte. Self-standing SPION/rGO paper was used as the working electrode without using any binder or current collector. SCE and graphite electrode were utilized as the reference and counter electrodes, respectively. CV measurements were performed between -0.8 V and 0.8 V (vs Ag/AgCl) at scan rates from 2 to 100 mV s^{-1}. A symmetric cell was assembled with two identical SPION/rGO papers for the calculation of energy and power density. The papers were immersed into the electrolyte solution (0.5 M

Na_2SO_4) for 4 hours before the preparation of 2-electrode cell. For the electrical contact, Au plates were placed at the edge of uncoated side of composite papers. Energy density (E) and power density (P) values are calculated according to the energy and power equations mentioned in section 3.3.2. .

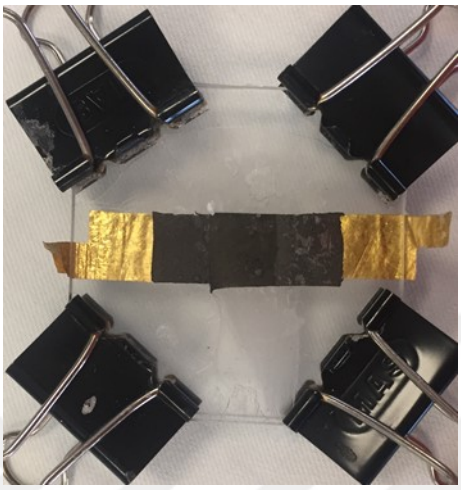

Figure 4-1: A symmetric cell with two identical SPION/rGO papers, gold current collectors and glassy fibrious separator

4.3. Results and Discussion

Digital images of composite papers show that these films have two different sides. While the side decorated with the Fe_3O_4 nanoparticles has dark red color (Figure 4-2b), the other side has shinny gray color (Figure 4-2a). In FESEM images, distributed nanoparticles were observed in SPION side, and negligible amount of nanoparticles were observed in rGO side (Figure 4-3a). The surface chemical structure was investigated with XPS. There are two intense peaks at 711.6 ($2p_{3/2}$) and 725.2 eV ($2p_{1/2}$) in Fe 2p spectrum (Figure 4-4a). These binding energies correspond to mixed valence state of Fe^{2+} and Fe^{3+}[159,160]. In C1s spectrum, the peak around 284 eV associated with C-C, C=C bonds has relatively higher intensity compared to peaks around 285, 286, and 287 eV which correspond to C-N, C-O, C=O bonds, respectively. It proves that the reduction of the paper was carried out successfully.

The surface chemical composition was also investigated with XPS. While rGO side of paper contains 1.2% Fe and 75.4% C, SPION side has 9.7% Fe and 21% C according to the fitted spectra. This result is also consistent with the FESEM images.

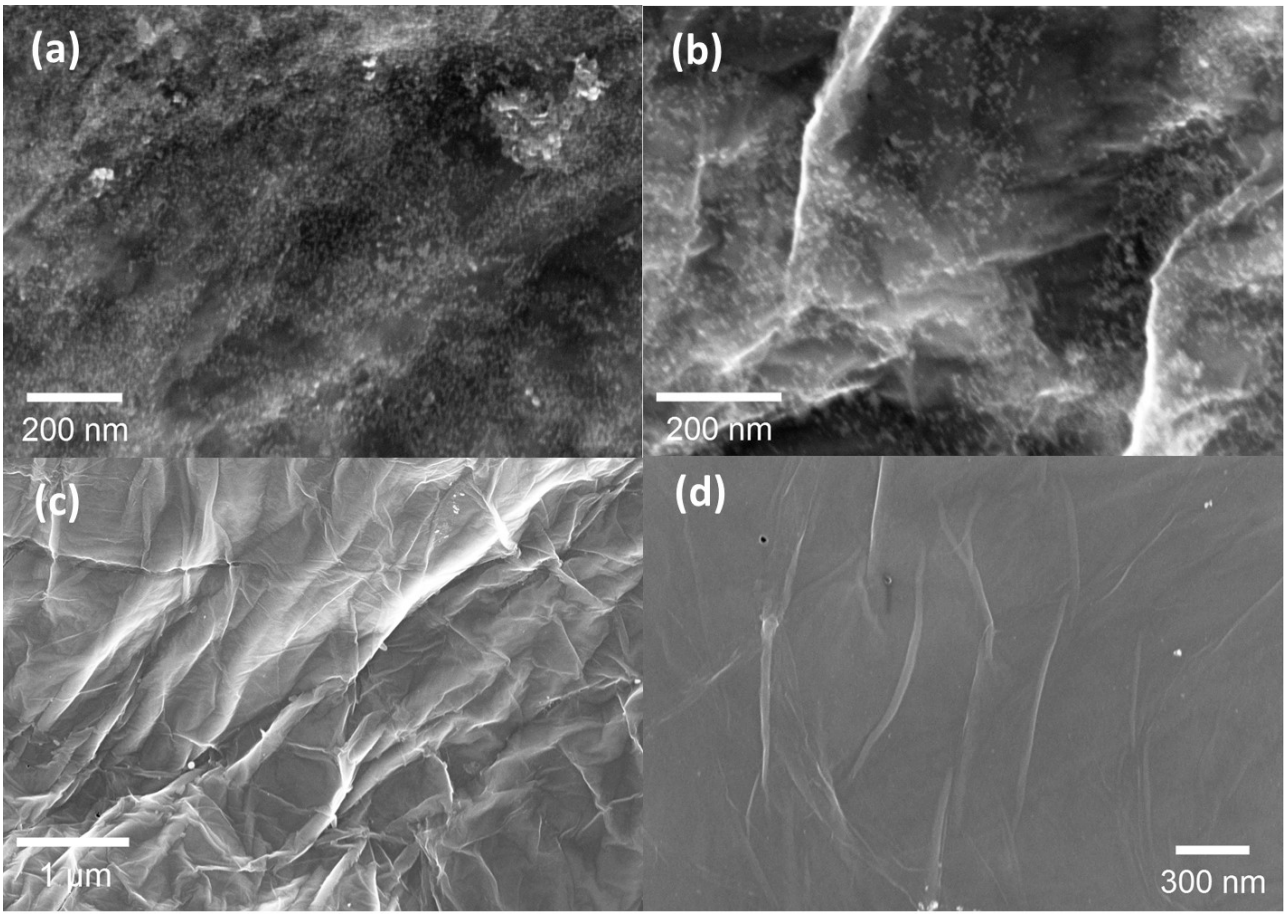

Figure 4-3: FESEM Images of (a,b) SPION side; (c,d) rGO side of SPION/rGO composite paper prepared via layering technique.

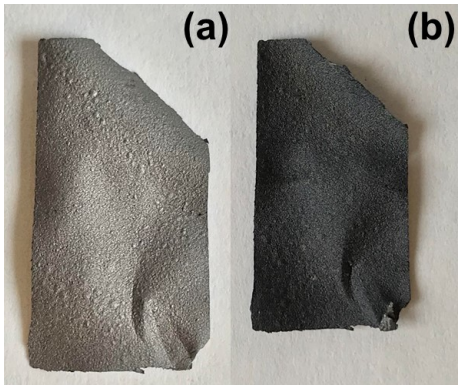

Figure 4-2:Digital image of (a) rGO side, (b) SPION side of Fe_3O_4/rGO paper.

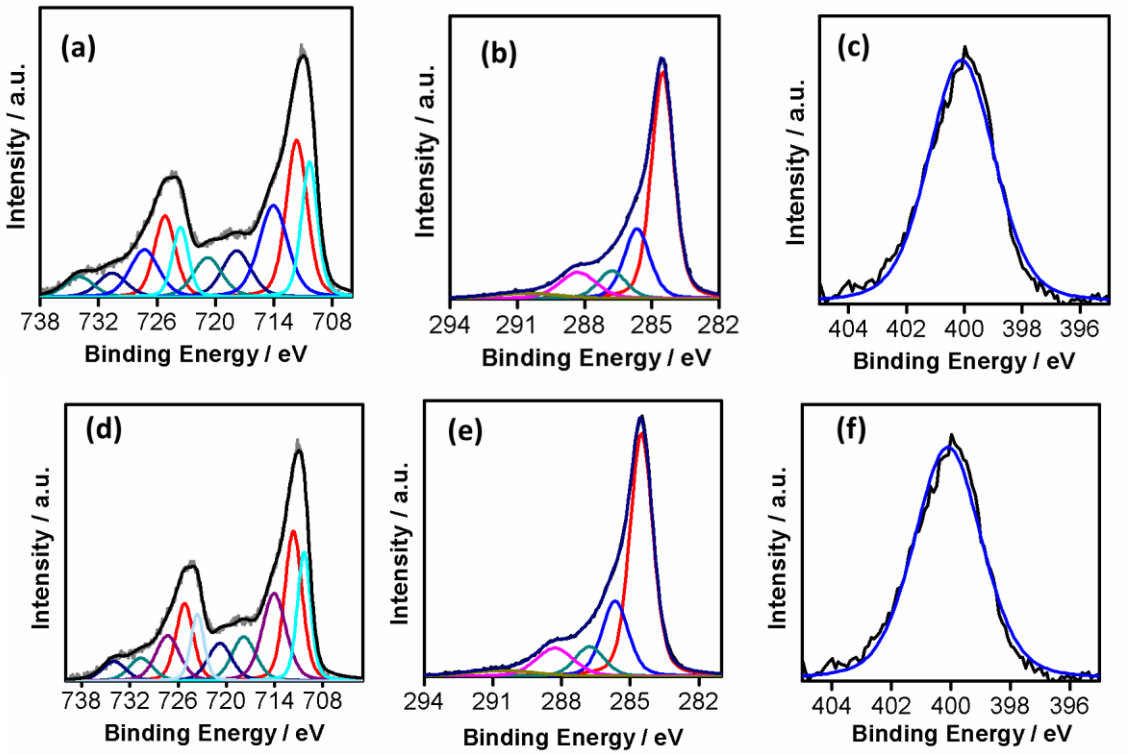

Figure 4-4: (a) Fe2p, (b) C1s, and (c) N1s XPS spectra of rGO side of composite paper; (d) Fe2p, (e) C1s, and (f) N1s XPS spectra of SPION side of composite paper.

Table 4-1: Atomic percentages calculated from the fitted spectra

Sample	**C**	**O**	**N**	**Fe**
SPION side	42.97	31.37	18.96	18.96
rGO side	74.79	14.03	8.66	2.62

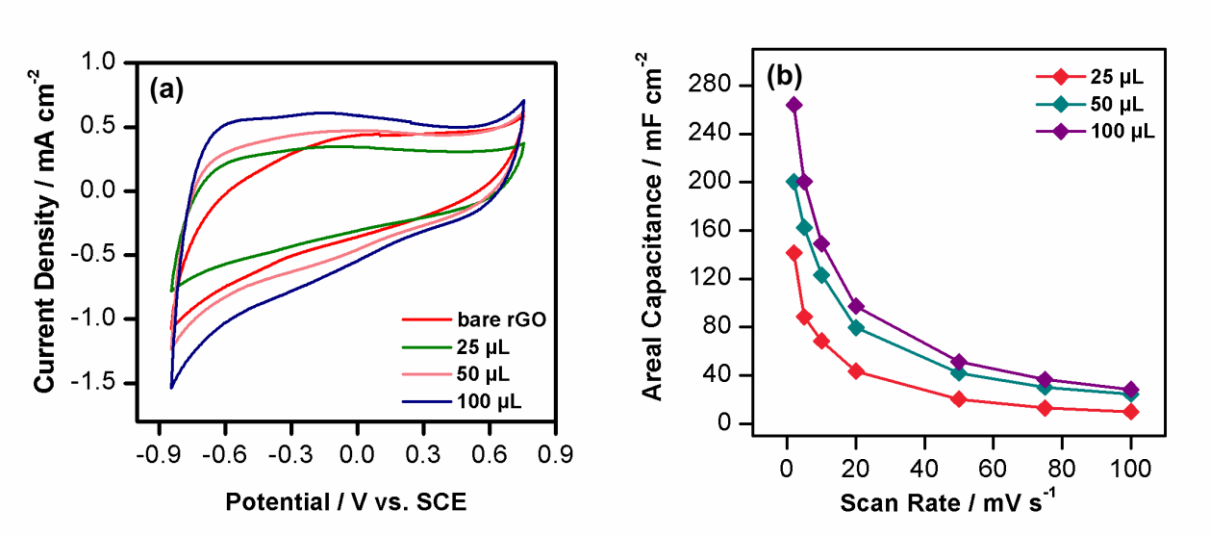

Figure 4-5: (a) CV curves of bare rGO, the composite with 25µL , 50 µL, and 100 µL SPION at the scan rate of 2mV s^{-1}; (b) Areal capacitances of composite papers with different amount of SPION at different scan rates

Table 4-2. Areal and specific capacitances calculated from CV curves of papers with 25 µL, 50 µL, and 100 µL SPION

Sample	Areal Capacitance	Specific Capacitance
25 uL SPION	141.7	80.9
50 uL SPION	200.6	112.0
100 uL SPION	263.9	101.5

Figure 4-5 shows CV curves of bare rGO and SPION/rGO composites with different amount of SPION. Corresponding areal and specific capacitances were shown in Table 4-2. It is seen that with the increasing amount of SPION, areal capacitance is increasing, but specific capacitances do not have the same trend since the mass of the composite increased drastically with 100 uL SPION. SPION/rGO composite with 50 µL SPION has the highest specific capacitance of 112.0 F g^{-1} at the scan rate of 2 mV s^{-1}. Electrochemical performances of composited prepared via mixing and layering were compared via CV at the scan rate of 2 mV s^{-1}. It is seen that voltammograms of the composites prepared via layering display symmetrical

small redox peaks and these samples have higher capacitances compared to composites prepared via mixing method, as expected. Since metal oxide nanoparticles on the surface can contribute to surface redox reactions, they can enhance the electrochemical performance [161].

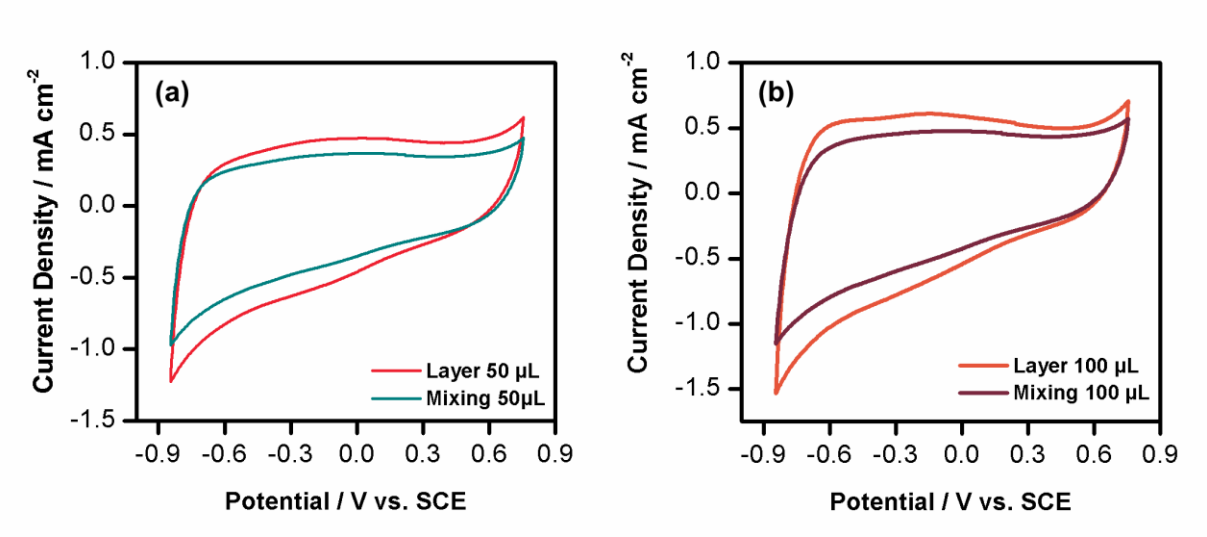

Figure 4-6: CV curves of (a) composites with 50 µL and (b) composites with 100 µL SPION via two different techniques

Table 4-3: Areal and specific capacitances of composite papers prepared via layering and mixing methods

Sample	Areal Capacitance mF cm^{-2}	Specific Capacitance / F g^{-1}
Layer 50 µL	200.6	112.0
Mixing 50 µL	166.1	94.9
Layer 100 µL	263.9	101.5
Mixing 100 µL	204.6	91.7

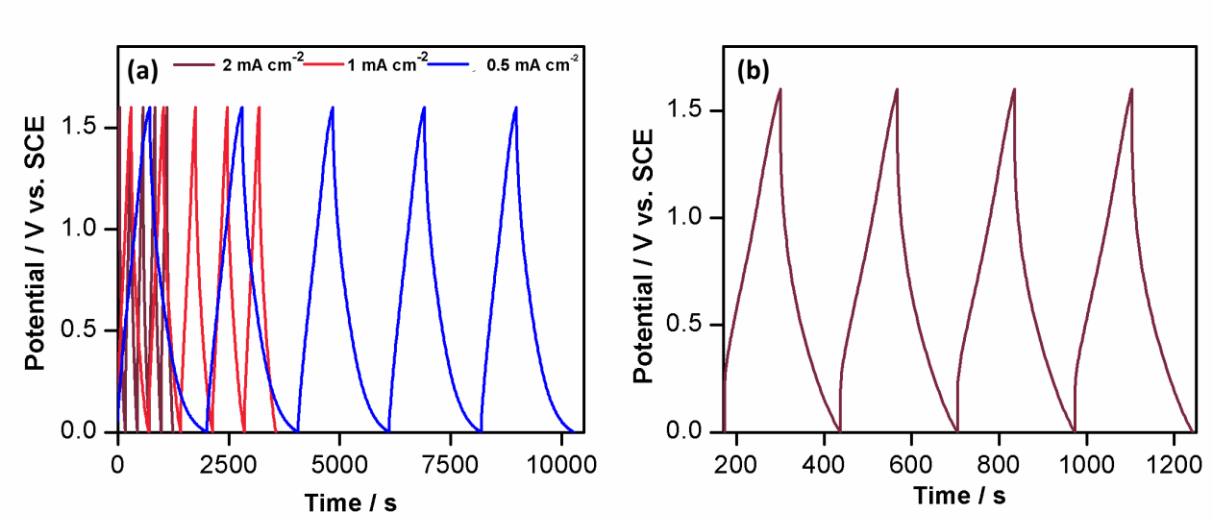

Figure 4-7: (a) GCD curves of the sample layer 50 µL at the current density 2, 1, and 0.5 mA cm^{-2}; (b) GCD curves of layer 50 µL at 2 mA cm^{-2}

Table 4-4: Specific capacitance values of layer 50 µL at different current densities and scan rates

Scan Rate / mV s-1	**Specific Capacitance /F g-1**	**Current Density /mA cm^{-2}**	**Specific Capacitance /F g-1**
10	68.7	2	88.7
5	90.7	1	121.1
2	112.1	0.5	203.4

Figure 4-8a displays CV curves of two-electrode cell over different potential ranges from 1.0 V to 1.5 V at the scan rate of 20 mV s^{-1}. The maximum operating cell voltage is 1.5 V without any significant distortion. Rectangular-like shape CV curves were observed at different scan rates without any redox peak which indicates ideal capacitive behavior. The current density is increasing with increasing scan rate (Figure 4-8b).

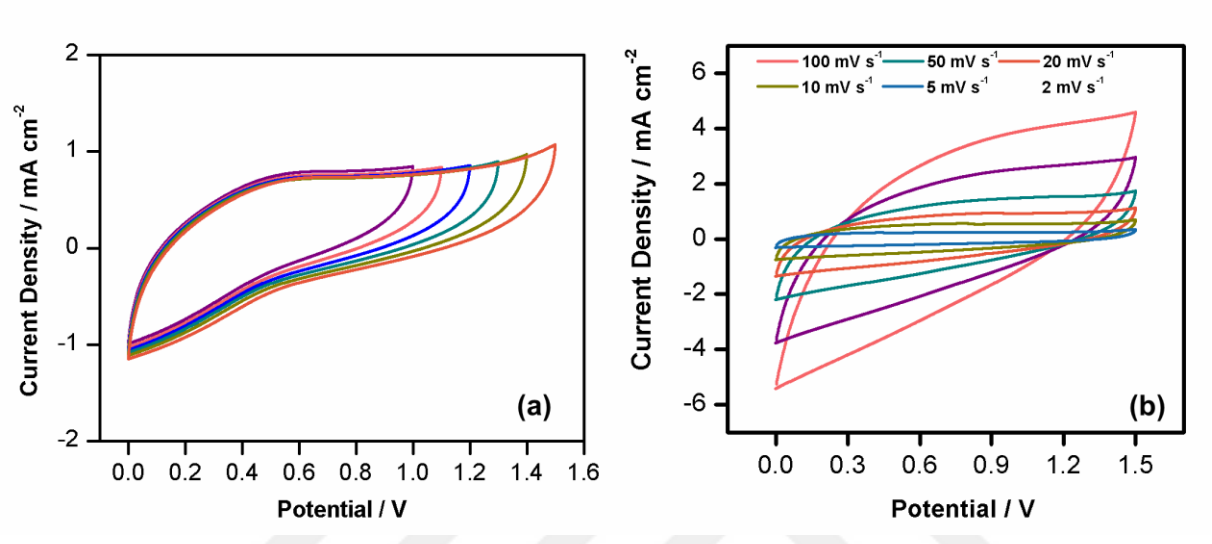

Figure 4-8:(a) CV curves of the symmetric cell at different operating potential windows; (b) CV curves of the cell at different scan rates.

Figure 4-9 a,b display CD curves of two-electrode cell at different current densities. Triangular shaped curves without obvious IR drop region were observed which associated with capacitive properties. Energy and power densities are calculated according to the discharge curve. While the highest power density was 375 W kg^{-1}, the highest energy density is 2.97 Wh kg^{-1}. Symmetric cell also exhibited high cyclic stability with 78% capacitance retention at 10000 cycles.

Corresponding energy efficiencies are calculated according to following equation:

$$n_E = \frac{Eint_D}{Eint_C}$$

where n_E is energy efficiency, $Eint_D$ is the area under the discharge curve and $Eint_C$ is the area under the charge curve. Although coulombic efficiency, in which charging and discharging times are utilized directly, is useful for ideal capacitors, calculating energy efficiency from the area under CD curves is useful for non-ideal cases [162].

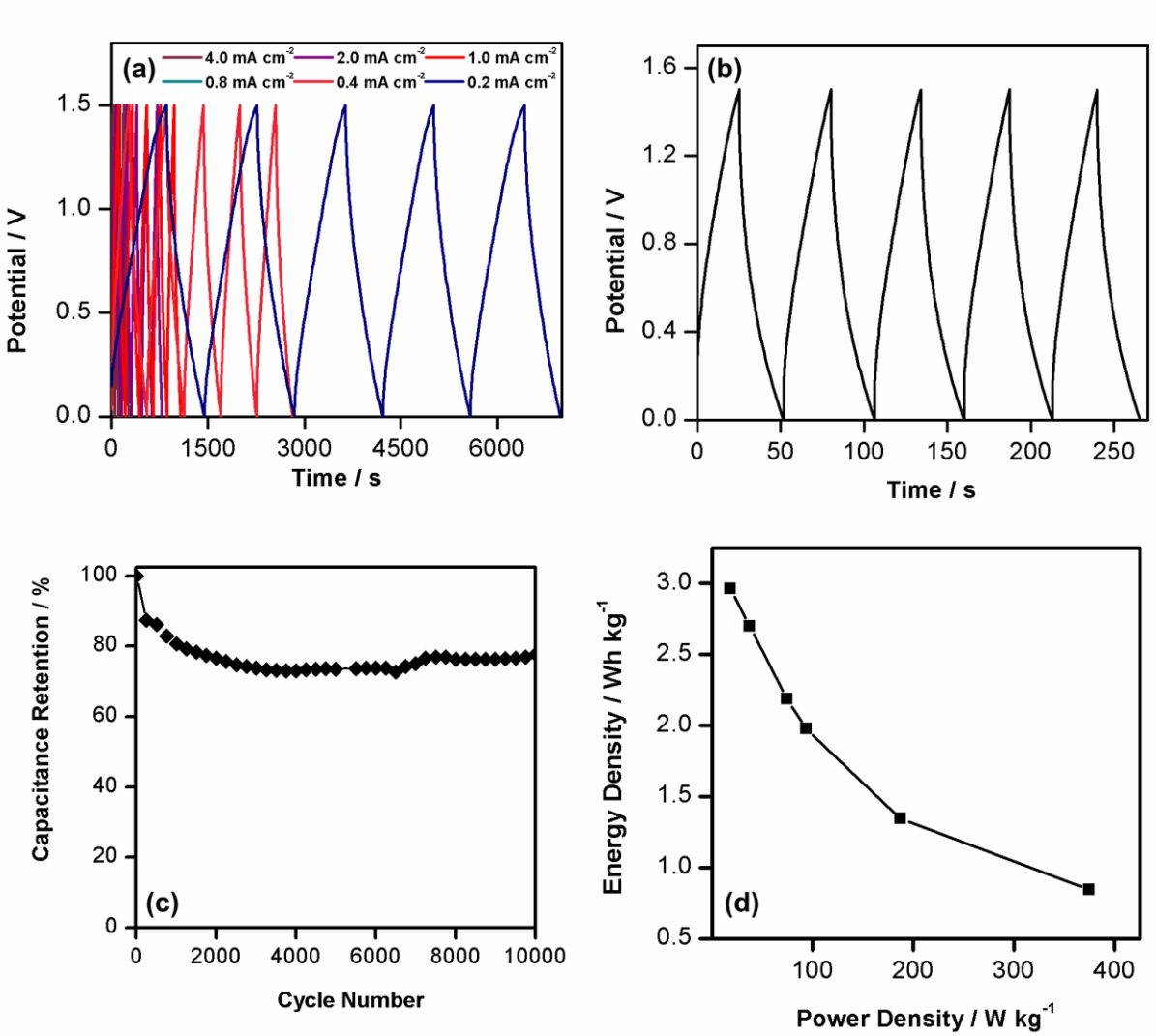

Figure 4-9: (a) GCD curves of the cell at different current densities of 4, 2, 1, 0.8, 0.4, and 0.2 mA cm^{-2}; (b) GCD curves of the cell at the highest current density of 4 mA cm^{-2}; (c) Capacitance retention at 10000 cycles of CV; (d) Ragone plot

Table 4-5. Energy and power densities of the symmetric cell

Current Density / mA cm^{-2}	Energy Density/ Wh kg^{-1}	Power Density W kg^{-1}	Energy Efficiency / %
4	0.84	375.0	37.5
2	1.34	187.5	45.3
1	1.98	93.8	46.4
0.8	2.19	75.0	47.1
0.4	2.70	37.5	47.1
0.2	2.97	18.8	42.0

4.4. Conclusion

In conclusion, rGO papers were decorated successfully with superparamagnetic iron oxide nanoparticles. Two different methods were utilized to prepare SPION/rGO composites and increasing amount of SPION enhances electrochemical performances. In GCD measurements, SPION/rGO electrode with 50 SPION showed the specific capacitance of 203 F g-1 at 0.5 mA cm-2. Furthermore, SPION/rGO composite achieved the operation potential window of 1.6 V in aqueous electrolyte along with high capacitance retention (78%) at 10000 cycles of CV.

Chapter 5: CONCLUSION

In this thesis, graphene oxide solution was successfully synthesized via modified Hummers' method. Self-standing and flexible graphene oxide papers were obtained via vacuum filtration method. Reduction of graphene oxide papers was performed via chemical reduction and thermal annealing to use as current collectors. Structural characterization of reduced graphene oxide papers was performed with XPS and Raman spectroscopy. Reduced graphene oxide papers were decorated with manganese oxide nanostructures by cathodic electrodeposition technique. Effects of different deposition potentials and mass loading on the morphology and electrochemical performances were evaluated. Mn_3O_4 phase of manganese oxide deposited at -1.1 V with mass loading 0.16 mg exhibited the highest specific capacitance of 546 F g^{-1} at 0.5 A g^{-1} in 0.5 M Na_2SO_4. During CV measurements, the phase transformation from Haussmannite phase to Birnessite phase of manganese oxide was observed.

In the last part, superparamagnetic iron oxide and reduced graphene oxide composite papers were prepared via two different techniques: mixing and layering. Papers prepared via layering method with 50 µL SPION solution achieved the highest specific capacitance of 112 F g^{-1}. Furthermore, SPION/rGO composites worked in wide potential range of 1.6 V along with high capacitance retention of 78% at 10000 cycles of cyclic voltammetry.

BIBLIOGRAPHY

[1] A.K. Geim, Graphene: status and prospects., Science. 324 (2009) 1530–4. http://www.ncbi.nlm.nih.gov/pubmed/19541989.

[2] R.K. Singh, R. Kumar, D.P. Singh, Graphene oxide: Strategies for synthesis, reduction and frontier applications, RSC Adv. 6 (2016) 64993–65011. doi:10.1039/c6ra07626b.

[3] K.S. Novoselov, A.K. Geim, S.V. Morozov, D. Jiang, Y. Zhang, S. v. Dubonos, I.V. Grigorieva, A.A. Firsov, Electric Field Effect in Atomically Thin Carbon Films, Science (80-.). 306 (2004) 666–669. doi:10.1126/science.1102896.

[4] A. Dato, V. Radmilovic, Z. Lee, J. Phillips, M. Frenklach, Substrate-Free Gas-Phase Synthesis of Graphene Sheets, Nano Lett. 8 (2008) 2012–2016. doi:10.1021/nl8011566.

[5] L.A. Galves, J.M. Wofford, G. V Soares, U. Jahn, C. Pfüller, H. Riechert, J.M.J. Lopes, The effect of the SiC (0001) surface morphology on the growth of epitaxial mono-layer graphene nanoribbons, Carbon N. Y. 115 (2017) 162–168. doi:10.1016/j.carbon.2017.01.018.

[6] K. Parvez, Z. Wu, R. Li, X. Liu, R. Graf, X. Feng, Exfoliation of Graphite into Graphene in Aqueous Solutions of Inorganic Salts, J. Am. Chem. Soc. 136 (2014) 6083–6091. doi:10.1021/ja5017156.

[7] C.H. Lui, L. Liu, K.F. Mak, G.W. Flynn, T.F. Heinz, Ultraflat graphene, Nature. 462 (2009) 339–341. doi:10.1038/nature08569.

[8] B.C. Brodie, Ueber das Atomgewicht des Graphits, Ann. Der Chemie Und Pharm. 114 (1860) 6–24. doi:10.1002/jlac.18601140103.

[9] W.S. Hummers, R.E. Offeman, Preparation of Graphitic Oxide, J. Am. Chem. Soc. 80 (1958) 1339–1339. doi:10.1021/ja01539a017.

[10] O.C. Compton, S.T. Nguyen, Graphene oxide, highly reduced graphene oxide, and

graphene: Versatile building blocks for carbon-based materials, Small. 6 (2010) 711–723. doi:10.1002/smll.200901934.

[11] O.C. Compton, S.T. Nguyen, Graphene Oxide, Highly Reduced Graphene Oxide, and Graphene: Versatile Building Blocks for Carbon-Based Materials, Small. 6 (2010) 711–723. doi:10.1002/smll.200901934.

[12] D.R. Dreyer, D. Todd, C.W. Bielawski, Harnessing the chemistry of graphene oxide, Chem. Soc. Rev. 43 (2014) 5288–5301. doi:10.1039/c4cs00060a.

[13] A.M. Dimiev, J.M. Tour, M. Science, C. Science, N. Science, M. Street, U. States, A.Z.E. Materials, M. Avenue, U. States, Mechanism of Graphene Oxide, ACS Nano. 8 (2014) 3060–3068. doi:10.1021/nn500606a.

[14] S. Eigler, A. Hirsch, Chemistry with Graphene and Graphene Oxide — Challenges for Synthetic Chemists Angewandte, (2014) 7720–7738. doi:10.1002/anie.201402780.

[15] W. Cai, R.D. Piner, F.J. Stadermann, S. Park, M.A. Shaibat, Y. Ishii, D. Yang, A. Velamakanni, S.J. An, M. Stoller, J. An, D. Chen, R.S. Ruoff, Synthesis and Solid-State NMR Structural Characterization of 13C-Labeled Graphite Oxide, Science (80-.). 321 (2008) 1815–1817. doi:10.1126/science.1162369.

[16] H. He, J. Klinowski, M. Forster, A. Lerf, A new structural model for graphite oxide, Chem. Phys. Lett. 287 (1998) 53–56.

[17] A. Lerf, H. He, M. Forster, J. Klinowski, Structure of Graphite Oxide Revisited ‖, J. Phys. Chem. B. 102 (1998) 4477–4482. doi:10.1021/jp9731821.

[18] B. Standley, A. Mendez, E. Schmidgall, M. Bockrath, Graphene-graphite oxide field-effect transistors, Nano Lett. 12 (2012) 1165–1169. doi:10.1021/nl2028415.

[19] M.P. Down, S.J. Rowley-Neale, G.C. Smith, C.E. Banks, Fabrication of Graphene Oxide Supercapacitor Devices, ACS Appl. Energy Mater. 1 (2018) 707–714. doi:10.1021/acsaem.7b00164.

[20] H. Xian, T. Peng, H. Sun, J. Wang, The Effect of Thermal Exfoliation Temperature on the Structure and Supercapacitive Performance of Graphene Nanosheets, Nano-Micro Lett. 7 (2015) 17–26. doi:10.1007/s40820-014-0014-4.

[21] D. Chen, H. Feng, J. Li, Graphene oxide: preparation, functionalization, and electrochemical applications., Chem. Rev. 112 (2012) 6027–53. doi:10.1021/cr300115g.

[22] M.D. Stoller, S. Park, Y. Zhu, J. An, R.S. Ruoff, Graphene-based ultracapacitors, Nano Lett. 8 (2008) 3498–502. doi:10.1021/nl802558y.

[23] C. Zhao, L. Xing, J. Xiang, L. Cui, J. Jiao, H. Sai, Formation of uniform reduced graphene oxide films on modified PET substrates using drop-casting method, Particuology. 17 (2014) 66–73. doi:10.1016/j.partic.2014.02.005.

[24] J. Zhu, J. He, Assembly and benign step-by-step post-treatment of oppositely charged reduced graphene oxides for transparent conductive thin films with multiple applications, Nanoscale. 4 (2012) 3558. doi:10.1039/c2nr30606a.

[25] S. Dae, J. Lee, T. Kim, K. Rana, J. Yeob, J. Hyeok, S.S. Yoon, J. Ahn, Additive-free electrode fabrication with reduced graphene oxide using supersonic kinetic spray for fl exible lithium-ion batteries, Carbon N. Y. 139 (2018) 195–204. doi:10.1016/j.carbon.2018.06.040.

[26] Fitrilawati, M.B. Perkasa, N. Syakir, A. Aprilia, L. Safriani, T. Saragi, Risdiana, S. Hidayat, A. Bahtiar, R. Siregar, R.R. Sihombing, A. Nugroho, Thermal Reduction Study of Graphene Oxide Paper, IOP Conf. Ser. Mater. Sci. Eng. 196 (2017). doi:10.1088/1757-899X/196/1/012027.

[27] H.A. Becerril, J. Mao, Z. Liu, R.M. Stoltenberg, Z. Bao, Y. Chen, Evaluation of Solution-Processed Reduced Graphene Oxide Films as Transparent Conductors, ACS Nano. 2 (2008) 463–470. doi:10.1021/nn700375n.

[28] Y. Shao, J. Wang, H. Wu, J. Liu, I.A. Aksay, Y. Lin, Graphene Based Electrochemical Sensors and Biosensors: A Review, Electroanalysis. 22 (2010) 1027–1036. doi:10.1002/elan.200900571.

[29] X. Ye, Y. Zhu, Z. Tang, Z. Wan, C. Jia, In-situ chemical reduction produced graphene paper for flexible supercapacitors with impressive capacitive performance, J. Power Sources. 360 (2017) 48–58. doi:10.1016/j.jpowsour.2017.05.103.

[30] D. Yang, A. Velamakanni, G. Bozoklu, S. Park, M. Stoller, R.D. Piner, S. Stankovich, I. Jung, D.A. Field, C.A. Ventrice, R.S. Ruoff, Chemical analysis of graphene oxide films after heat and chemical treatments by X-ray photoelectron and Micro-Raman spectroscopy, Carbon N. Y. 47 (2009) 145–152. doi:10.1016/j.carbon.2008.09.045.

[31] T. Nakamura, S. Sato, Photochemical reduction of graphene oxide (GO) by femtosecond laser irradiation, in: U. Klotzbach, K. Washio, C.B. Arnold (Eds.), 2016: p. 973617. doi:10.1117/12.2211583.

[32] D. Voiry, R. Fullon, C. Lee, H.Y. Jeong, H.S. Shin, M. Chhowalla, High-quality graphene via microwave reduction of solution-exfoliated graphene oxide, Science (80-.). 353 (2016) 1430–1433.

[33] J. Kauppila, P. Kunnas, P. Damlin, A. Viinikanoja, C. Kvarnström, Electrochemical reduction of graphene oxide films in aqueous and organic solutions, Electrochim. Acta. 89 (2013) 84–89. doi:10.1016/j.electacta.2012.10.153.

[34] H.-B. Zhang, J.-W. Wang, Q. Yan, W.-G. Zheng, C. Chen, Z.-Z. Yu, Vacuum-assisted synthesis of graphene from thermal exfoliation and reduction of graphite oxide, J. Mater. Chem. 21 (2011) 5392. doi:10.1039/c1jm10099h.

[35] X. Li, H. Wang, J.T. Robinson, H. Sanchez, G. Diankov, H. Dai, Simultaneous Nitrogen Doping and Reduction of Graphene Oxide, J. Am. Chem. Soc. (2009) 15939–15944. doi:10.1021/ja907098f.

[36] S. Pei, H. Cheng, The reduction of graphene oxide, Carbon N. Y. 50 (2011) 3210–3228. doi:10.1016/j.carbon.2011.11.010.

[37] H.J. Shin, K.K. Kim, A. Benayad, S.M. Yoon, H.K. Park, I.S. Jung, M.H. Jin, H.K. Jeong, J.M. Kim, J.Y. Choi, Y.H. Lee, Efficient reduction of graphite oxide by sodium borohydride and its effect on electrical conductance, Adv. Funct. Mater. 19 (2009) 1987–1992. doi:10.1002/adfm.200900167.

[38] J. Zhang, H. Yang, G. Shen, P. Cheng, Reduction of graphene oxide via L-ascorbic acid, Chem. Commun. 46 (2010) 1112–1114. doi:10.1039/b917705a.

[39] A.K. Das, M. Srivastav, R.K. Layek, M.E. Uddin, D. Jung, N.H. Kim, J.H. Lee, Iodide-mediated room temperature reduction of graphene oxide: A rapid chemical route for the synthesis of a bifunctional electrocatalyst, J. Mater. Chem. A. 2 (2014) 1332–1340. doi:10.1039/c3ta13688d.

[40] Z. Lei, L. Lu, X.S. Zhao, The electrocapacitive properties of graphene oxide reduced by urea, Energy Environ. Sci. 5 (2012) 6391–6399. doi:10.1039/C1EE02478G.

[41] S. Park, J. An, J.R. Potts, A. Velamakanni, S. Murali, R.S. Ruoff, Hydrazine-reduction of graphite- and graphene oxide, Carbon N. Y. 49 (2011) 3019–3023. doi:10.1016/j.carbon.2011.02.071.

[42] S. Stankovich, D.A. Dikin, R.D. Piner, K.A. Kohlhaas, A. Kleinhammes, Y. Jia, Y. Wu, S.T. Nguyen, R.S. Ruoff, Synthesis of graphene-based nanosheets via chemical reduction of exfoliated graphite oxide, Carbon N. Y. 45 (2007) 1558–1565. doi:10.1016/j.carbon.2007.02.034.

[43] M.C. Kim, G.S. Hwang, R.S. Ruoff, Epoxide reduction with hydrazine on graphene: A first principles study, J. Chem. Phys. 131 (2009) 064704. doi:10.1063/1.3197007.

[44] X. Gao, J. Jang, S. Nagase, Hydrazine and Thermal Reduction of Graphene Oxide : Reaction Mechanisms , Product Structures , and Reaction Design, J. Phys. Chem. C.

114 (2010) 832–842. doi:10.1021/jp909284g.

[45] L. Zhang, X. Hu, Z. Wang, F. Sun, D.G. Dorrell, A review of supercapacitor modeling, estimation, and applications: A control/management perspective, Renew. Sustain. Energy Rev. 81 (2018) 1868–1878. doi:10.1016/j.rser.2017.05.283.

[46] A. Muzaffar, M.B. Ahamed, K. Deshmukh, J. Thirumalai, A review on recent advances in hybrid supercapacitors: Design, fabrication and applications, Renew. Sustain. Energy Rev. 101 (2019) 123–145. doi:10.1016/j.rser.2018.10.026.

[47] G. Wang, L. Zhang, J. Zhang, A review of electrode materials for electrochemical supercapacitors, Chem. Soc. Rev. 41 (2012) 797–828. doi:10.1039/C1CS15060J.

[48] T. Chen, L. Dai, Flexible supercapacitors based on carbon nanomaterials, J. Mater. Chem. A. 2 (2014) 10756–10775. doi:10.1039/c4ta00567h.

[49] W.K. Chee, H.N. Lim, Z. Zainal, N.M. Huang, I. Harrison, Y. Andou, Flexible Graphene-Based Supercapacitors: A Review, J. Phys. Chem. C. 120 (2016) 4153–4172. doi:10.1021/acs.jpcc.5b10187.

[50] V. Augustyn, P. Simon, B. Dunn, Pseudocapacitive oxide materials for high-rate electrochemical energy storage, Energy Environ. Sci. 7 (2014) 1597. doi:10.1039/c3ee44164d.

[51] T. Brousse, B. Daniel, To Be or Not To Be Pseudocapacitive ?, 162 (2015) 5185–5189. doi:10.1149/2.0201505jes.

[52] J. Liu, J. Wang, C. Xu, H. Jiang, C. Li, L. Zhang, J. Lin, Z.X. Shen, Advanced Energy Storage Devices: Basic Principles, Analytical Methods, and Rational Materials Design, Adv. Sci. 5 (2018) 1700322. doi:10.1002/advs.201700322.

[53] C. Zhan, D. Jiang, Understanding the pseudocapacitance of RuO 2 from joint density functional theory, J. Phys. Condens. Matter. 28 (2016) 464004. doi:10.1088/0953-8984/28/46/464004.

[54] I. Ryu, G. Kim, H. Yoon, S.J. Ahn, S. Yim, Hierarchically nanostructured MnO2electrodes for pseudocapacitor application, RSC Adv. 6 (2016) 102814–102820. doi:10.1039/c6ra22841k.

[55] C.-C. Chen, C.-Y. Chen, C.-Y. Tsay, S.-Y. Wang, C.-K. Lin, Influence of Fe3O4 nanoparticles on pseudocapacitive behavior of the charge storage process, J. Alloys Compd. 645 (2015) 250–258. doi:10.1016/j.jallcom.2015.04.123.

[56] F.E. Sarac, U. Unal, Electrochemical-Hydrothermal Synthesis of Manganese Oxide Films as Electrodes for Electrochemical Capacitors, Electrochim. Acta. 178 (2015) 199–208. doi:10.1016/j.electacta.2015.07.169.

[57] G. Xiong, K.P.S.S. Hembram, R.G. Reifenberger, T.S. Fisher, MnO 2 -coated graphitic petals for supercapacitor electrodes, J. Power Sources. 227 (2013) 254–259. doi:10.1016/j.jpowsour.2012.11.040.

[58] X. Wu, J. Tang, Y. Duan, A. Yu, R.M. Berry, K.C. Tam, Conductive cellulose nanocrystals with high cycling stability for supercapacitor applications, J. Mater. Chem. A. 2 (2014) 19268–19274. doi:10.1039/C4TA04929B.

[59] S. Sahoo, S. Dhibar, G. Hatui, P. Bhattacharya, C.K. Das, Graphene/polypyrrole nanofiber nanocomposite as electrode material for electrochemical supercapacitor, Polymer (Guildf). 54 (2013) 1033–1042. doi:10.1016/j.polymer.2012.12.042.

[60] C. Zhong, Y. Deng, W. Hu, J. Qiao, L. Zhang, J. Zhang, A review of electrolyte materials and compositions for electrochemical supercapacitors, Chem. Soc. Rev. 44 (2015) 7484–7539. doi:10.1039/C5CS00303B.

[61] P.L. Taberna, C. Portet, P. Simon, Electrode surface treatment and electrochemical impedance spectroscopy study on carbon/carbon supercapacitors, Appl. Phys. A. 82 (2006) 639–646. doi:10.1007/s00339-005-3404-0.

[62] Z. Stević, M. Vujasinović, M. Radunović, Estimation of Parameters Obtained by

Electrochemical Impedance Spectroscopy on Systems Containing High Capacities, Sensors. 9 (2009) 7365–7373. doi:10.3390/s90907365.

[63] Q. Xue, J. Sun, Y. Huang, M. Zhu, Z. Pei, H. Li, Y. Wang, N. Li, H. Zhang, C. Zhi, Recent Progress on Flexible and Wearable Supercapacitors, Small. 13 (2017) 1701827. doi:10.1002/smll.201701827.

[64] X. Li, Y. Tang, J. Song, W. Yang, M. Wang, C. Zhu, W. Zhao, J. Zheng, Y. Lin, Self-supporting activated carbon/carbon nanotube/reduced graphene oxide flexible electrode for high performance supercapacitor, Carbon N. Y. 129 (2018) 236–244. doi:10.1016/j.carbon.2017.11.099.

[65] C. Ma, X. Wang, Y. Ma, J. Sheng, Y. Li, S. Li, J. Shi, Carbon nanofiber/graphene composite paper for flexible supercapacitors with high volumetric capacitance, Mater. Lett. 145 (2015) 197–200. doi:10.1016/j.matlet.2015.01.106.

[66] A. Khosrozadeh, M.A. Darabi, M. Xing, Q. Wang, Flexible Electrode Design: Fabrication of Freestanding Polyaniline-Based Composite Films for High-Performance Supercapacitors, ACS Appl. Mater. Interfaces. 8 (2016) 11379–11389. doi:10.1021/acsami.5b11256.

[67] L. Ma, R. Liu, H. Niu, L. Xing, L. Liu, Y. Huang, Flexible and Freestanding Supercapacitor Electrodes Based on Nitrogen-Doped Carbon Networks/Graphene/Bacterial Cellulose with Ultrahigh Areal Capacitance, ACS Appl. Mater. Interfaces. 8 (2016) 33608–33618. doi:10.1021/acsami.6b11034.

[68] X. Cui, R. Lv, R.U.R. Sagar, C. Liu, Z. Zhang, Reduced graphene oxide/carbon nanotube hybrid film as high performance negative electrode for supercapacitor, Electrochim. Acta. 169 (2015) 342–350. doi:10.1016/j.electacta.2015.04.074.

[69] W. Kong, K. Yao, X. Duan, Z. Liu, J. Hu, Holey Co, N-codoped graphene aerogel with in-plane pores and multiple active sites for efficient oxygen reduction, Electrochim.

Acta. 269 (2018) 544–552. doi:10.1016/j.electacta.2018.02.148.

[70] H.J. Choi, S.M. Jung, J.M. Seo, D.W. Chang, L. Dai, J.B. Baek, Graphene for energy conversion and storage in fuel cells and supercapacitors, Nano Energy. 1 (2012) 534–551. doi:10.1016/j.nanoen.2012.05.001.

[71] B. Mendoza-Sánchez, B. Rasche, V. Nicolosi, P.S. Grant, Scaleable ultra-thin and high power density graphene electrochemical capacitor electrodes manufactured by aqueous exfoliation and spray deposition, Carbon N. Y. 52 (2013) 337–346. doi:10.1016/j.carbon.2012.09.035.

[72] Y. Xiao, Z. Xu, Y. Liu, L. Peng, J. Xi, B. Fang, F. Guo, P. Li, C. Gao, Sheet Collapsing Approach for Rubber-like Graphene Papers, ACS Nano. 11 (2017) 8092–8102. doi:10.1021/acsnano.7b02915.

[73] M.M. Jaafar, G.P.M.K. Ciniciato, S.A. Ibrahim, S.M. Phang, K. Yunus, A.C. Fisher, M. Iwamoto, P. Vengadesh, Preparation of a Three-Dimensional Reduced Graphene Oxide Film by Using the Langmuir-Blodgett Method, Langmuir. 31 (2015) 10426–10434. doi:10.1021/acs.langmuir.5b02708.

[74] S.J. Chang, M.S. Hyun, S. Myung, M.A. Kang, J.H. Yoo, K.G. Lee, B.G. Choi, Y. Cho, G. Lee, T.J. Park, Graphene growth from reduced graphene oxide by chemical vapour deposition: Seeded growth accompanied by restoration, Sci. Rep. 6 (2016) 1–9. doi:10.1038/srep22653.

[75] G. Ning, C. Xu, Y. Cao, X. Zhu, Z. Jiang, Z. Fan, W. Qian, F. Wei, J. Gao, Chemical vapor deposition derived flexible graphene paper and its application as high performance anodes for lithium rechargeable batteries, J. Mater. Chem. A. 1 (2013) 408–414. doi:10.1039/C2TA00140C.

[76] C. Chen, Q.H. Yang, Y. Yang, W. Lv, Y. Wen, P.X. Hou, M. Wang, H.M. Cheng, Self-assembled free-standing graphite oxide membrane, Adv. Mater. 21 (2009) 3007–

3011. doi:10.1002/adma.200803726.

[77] D. a Dikin, S. Stankovich, E.J. Zimney, R.D. Piner, G.H.B. Dommett, G. Evmenenko, S.T. Nguyen, R.S. Ruoff, Preparation and characterization of graphene oxide paper., Nature. 448 (2007) 457–460. doi:10.1038/nature06016.

[78] O. Sadak, A.K. Sundramoorthy, S. Gunasekaran, Facile and green synthesis of highly conductive graphene paper, Carbon N. Y. 138 (2018) 108–117. doi:10.1016/j.carbon.2018.05.076.

[79] H. Gwon, H. Kim, K.U. Lee, D. Seo, Y.C. Park, Y. Lee, B.T. Ahn, K. Kang, Flexible energy storage devices based on graphene paper, Energy Environ. Sci. 4 (2011) 1277. doi:10.1039/c0ee00640h.

[80] G.A. Ferrero, M. Sevilla, A.B. Fuertes, Flexible, Free-Standing and Holey Graphene Paper for High-Power Supercapacitors, ChemNanoMat. 2 (2016) 1055–1063. doi:10.1002/cnma.201600228.

[81] Q. Li, X. Guo, Y. Zhang, W. Zhang, C. Ge, L. Zhao, X. Wang, H. Zhang, J. Chen, Z. Wang, L. Sun, Porous graphene paper for supercapacitor applications, J. Mater. Sci. Technol. 33 (2017) 793–799. doi:10.1016/j.jmst.2017.03.018.

[82] D. He, A.J. Marsden, Z. Li, R. Zhao, W. Xue, M.A. Bissett, Fabrication of a Graphene-Based Paper-Like Electrode for Flexible Solid-State Supercapacitor Devices, J. Electrochem. Soc. 165 (2018) A3481–A3486. doi:10.1149/2.1041814jes.

[83] Y. Gao, Y. Zhang, Y. Zhang, L. Xie, X. Li, F. Su, X. Wei, Z. Xu, C. Chen, R. Cai, Three-dimensional paper-like graphene framework with highly orientated laminar structure as binder-free supercapacitor electrode, J. Energy Chem. 25 (2016) 49–54. doi:10.1016/j.jechem.2015.11.011.

[84] F.E. Sarac Oztuna, S.B. Barim, S.E. Bozbag, H. Yu, M. Aindow, U. Unal, C. Erkey, Graphene Aerogel Supported Pt Electrocatalysts for Oxygen Reduction Reaction by

Supercritical Deposition, Electrochim. Acta. 250 (2017) 174–184. doi:10.1016/j.electacta.2017.08.067.

[85] P. Bhawal, S. Ganguly, T.K. Chaki, N.C. Das, Synthesis and characterization of graphene oxide filled ethylene methyl acrylate hybrid nanocomposites, RSC Adv. 6 (2016) 20781–20790. doi:10.1039/C5RA24914G.

[86] F.E. Sarac Oztuna, M.B. Yagci, U. Unal, First-Row Transition-Metal Cations (Co 2+ , Ni 2+ , Mn 2+ , Fe 2+) and Graphene (Oxide) Composites: From Structural Properties to Electrochemical Applications, Chem. – A Eur. J. (2019) chem.201806309. doi:10.1002/chem.201806309.

[87] A. Ganguly, S. Sharma, P. Papakonstantinou, J. Hamilton, Probing the Thermal Deoxygenation of Graphene Oxide Using High-Resolution In Situ X-ray-Based Spectroscopies, J. Phys. Chem. C. 115 (2011) 17009–17019. doi:10.1021/jp203741y.

[88] Y.N. Singhbabu, P. Kumari, S. Parida, R.K. Sahu, Conversion of pyrazoline to pyrazole in hydrazine treated N-substituted reduced graphene oxide films obtained by ion bombardment and their electrical properties, Carbon N. Y. 74 (2014) 32–43. doi:10.1016/j.carbon.2014.02.079.

[89] S. Park, Y. Hu, J.O. Hwang, E.-S. Lee, L.B. Casabianca, W. Cai, J.R. Potts, H.-W. Ha, S. Chen, J. Oh, S.O. Kim, Y.-H. Kim, Y. Ishii, R.S. Ruoff, Chemical structures of hydrazine-treated graphene oxide and generation of aromatic nitrogen doping, Nat. Commun. 3 (2012) 638. doi:10.1038/ncomms1643.

[90] A.C. Ferrari, J. Robertson, Interpretation of Raman spectra of disordered and amorphous carbon, Phys. Rev. B. 61 (2000) 14095–14107. doi:10.1103/PhysRevB.61.14095.

[91] S. Claramunt, A. Varea, D. López-Díaz, M.M. Velázquez, A. Cornet, A. Cirera, The importance of interbands on the interpretation of the raman spectrum of graphene

oxide, J. Phys. Chem. C. 119 (2015) 10123–10129. doi:10.1021/acs.jpcc.5b01590.

[92] M.A. Pimenta, G. Dresselhaus, M.S. Dresselhaus, L.G. Cançado, A. Jorio, R. Saito, Studying disorder in graphite-based systems by Raman spectroscopy, Phys. Chem. Chem. Phys. 9 (2007) 1276–1291. doi:10.1039/b613962k.

[93] S. Vollebregt, R. Ishihara, F.D. Tichelaar, Y. Hou, C.I.M. Beenakker, Influence of the growth temperature on the first and second-order Raman band ratios and widths of carbon nanotubes and fibers, Carbon N. Y. 50 (2012) 3542–3554. doi:10.1016/j.carbon.2012.03.026.

[94] T.V. Cuong, V.H. Pham, Q.T. Tran, S.H. Hahn, J.S. Chung, E.W. Shin, E.J. Kim, Photoluminescence and Raman studies of graphene thin films prepared by reduction of graphene oxide, Mater. Lett. 64 (2010) 399–401. doi:10.1016/j.matlet.2009.11.029.

[95] M. Yu, B. Xie, Y. Yang, Y. Zhang, Y. Chen, W. Yu, Residual oxygen groups in nitrogen-doped graphene to enhance the capacitive performance †, RSC Adv. 7 (2017) 15293–15301. doi:10.1039/c6ra28596a.

[96] Y. Joon, J. Joon, Y. Il, J. Kook, H. Na, J. Kim, S. Bin, Oxygen functional groups and electrochemical capacitive behavior of incompletely reduced graphene oxides as a thin-film electrode of supercapacitor, Electrochim. Acta. 116 (2014) 118–128. doi:10.1016/j.electacta.2013.11.040.

[97] M. Koinuma, H. Tateishi, K. Hatakeyama, S. Miyamoto, C. Ogata, A. Funatsu, T. Taniguchi, Y. Matsumoto, Analysis of Reduced Graphene Oxides by X-ray Photoelectron Spectroscopy and Electrochemical Capacitance, Chem. Lett. 42 (2013) 924–926. doi:10.1246/cl.130152.

[98] T. Beyazay, F. Eylul Sarac Oztuna, U. Unal, Self-Standing Reduced Graphene Oxide Papers Electrodeposited with Manganese Oxide Nanostructures as Electrodes for Electrochemical Capacitors, Electrochim. Acta. 296 (2019) 916–924.

doi:10.1016/j.electacta.2018.11.033.

[99] Y. Wang, Y. Song, Y. Xia, Electrochemical capacitors: mechanism, materials, systems, characterization and applications, Chem. Soc. Rev. 45 (2016) 5925–5950. doi:10.1039/C5CS00580A.

[100] L. Shen, L. Du, S. Tan, Z. Zang, C. Zhao, W. Mai, Flexible electrochromic supercapacitor hybrid electrodes based on tungsten oxide films and silver nanowires, Chem. Commun. 52 (2016) 6296–6299. doi:10.1039/c6cc01139j.

[101] Y. Sun, Q. Wu, G. Shi, Graphene based new energy materials, Energy Environ. Sci. 4 (2011) 1113. doi:10.1039/c0ee00683a.

[102] L. Ji, P. Meduri, V. Agubra, X. Xiao, M. Alcoutlabi, Graphene-Based Nanocomposites for Energy Storage, Adv. Energy Mater. 6 (2016) 1502159. doi:10.1002/aenm.201502159.

[103] H. Choi, H. Yoon, Nanostructured Electrode Materials for Electrochemical Capacitor Applications, Nanomaterials. 5 (2015) 906–936. doi:10.3390/nano5020906.

[104] S.K. Mondal, N. Munichandraiah, Anodic deposition of porous RuO2 on stainless steel for supercapacitor studies at high current densities, J. Power Sources. 175 (2008) 657–663. doi:10.1016/j.jpowsour.2007.08.104.

[105] Z. Chen, Pseudocapacitors Based on Hierarchically Porous Nanowire Composites, ACS Nano. (2012) 4319–4327. doi:10.1021/nn300920e.

[106] T. Brezesinski, J. Wang, S.H. Tolbert, B. Dunn, Ordered mesoporous alpha-MoO3 with iso-oriented nanocrystalline walls for thin-film pseudocapacitors, Nat. Mater. 9 (2010) 146–151. doi:10.1038/nmat2612.

[107] X. Xia, J. Tu, X. Wang, C. Gu, X. Zhao, Mesoporous Co3O4 monolayer hollow-sphere array as electrochemical pseudocapacitor material, Chem. Commun. 47 (2011) 5786–5788. doi:10.1039/c1cc11281c.

[108] T. Brousse, M. Toupin, R. Dugas, L. Athouël, O. Crosnier, D. Bélanger, Crystalline MnO2 as Possible Alternatives to Amorphous Compounds in Electrochemical Supercapacitors, J. Electrochem. Soc. 153 (2006) A2171–A2180. doi:10.1149/1.2352197.

[109] T. Brezesinski, J. Wang, J. Polleux, B. Dunn, S.H. Tolbert, Templated Nanocrystal-Based Porous TiO2 Films for Next-Generation Electrochemical Capacitors, J. Am. Chem. Soc. 131 (2009) 1802–1809. doi:10.1021/ja8057309.

[110] V. Augustyn, P. Simon, B. Dunn, Pseudocapacitive oxide materials for high-rate electrochemical energy storage, Energy Environ. Sci. 7 (2014) 1597. doi:10.1039/c3ee44164d.

[111] M.-S. Balogun, W. Qiu, W. Wang, P. Fang, X. Lu, Y. Tong, Recent advances in metal nitrides as high-performance electrode materials for energy storage devices, J. Mater. Chem. A. 3 (2015) 1364–1387. doi:10.1039/C4TA05565A.

[112] L.L. Zhang, R. Zhou, X.S. Zhao, Graphene-based materials as supercapacitor electrodes, J. Mater. Chem. 20 (2010) 5983. doi:10.1039/c000417k.

[113] Y. He, W. Chen, X. Li, Z. Zhang, J. Fu, C. Zhao, E. Xie, Freestanding Three-Dimensional Graphene/MnO 2 Composite Networks As Ultralight and Flexible Supercapacitor Electrodes, ACS Nano. 7 (2013) 174–182. doi:10.1021/nn304833s.

[114] M.S. Balogun, Y. Zeng, W. Qiu, Y. Luo, A. Onasanya, T.K. Olaniyi, Y. Tong, Three-dimensional nickel nitride (Ni3N) nanosheets: Free standing and flexible electrodes for lithium ion batteries and supercapacitors, J. Mater. Chem. A. 4 (2016) 9844–9849. doi:10.1039/c6ta02492k.

[115] A. Sumboja, C.Y. Foo, X. Wang, P.S. Lee, Large areal mass, flexible and free-standing reduced graphene oxide/manganese dioxide paper for asymmetric supercapacitor device, Adv. Mater. 25 (2013) 2809–2815. doi:10.1002/adma.201205064.

[116] Z. Li, J. Wang, X. Liu, S. Liu, J. Ou, S. Yang, Electrostatic layer-by-layer self-assembly multilayer films based on graphene and manganese dioxide sheets as novel electrode materials for supercapacitors, J. Mater. Chem. 21 (2011) 3397–3403. doi:10.1039/C0JM02650F.

[117] K. Neishi, S. Aki, K. Matsumoto, H. Sato, H. Itoh, S. Hosaka, J. Koike, K. Neishi, S. Aki, K. Matsumoto, H. Sato, H. Itoh, Formation of a manganese oxide barrier layer with thermal chemical vapor deposition for advanced large-scale integrated interconnect structure, Appl. Phys. Lett. 032106 (2012) 1–4. doi:10.1063/1.2963984.

[118] Y. Wang, I. Zhitomirsky, Electrophoretic Deposition of Manganese Dioxide - Multiwalled Carbon Nanotube Composites for Electrochemical Supercapacitors, Langmuir. 25 (2009) 9684–9689. doi:10.1021/la900937e.

[119] H. Xia, M.O. Lai, L. Lu, Nanostructured manganese oxide thin films as electrode material for supercapacitors, JOM. 63 (2011) 54–59. doi:10.1007/s11837-011-0014-5.

[120] M.S. Wu, Z.S. Guo, J.J. Jow, Highly regulated electrodeposition of needle-like manganese oxide nanofibers on carbon fiber fabric for electrochemical capacitors, J. Phys. Chem. C. 114 (2010) 21861–21867. doi:10.1021/jp108598q.

[121] L. Hu, W. Chen, X. Xie, N. Liu, Y. Yang, H. Wu, Y. Yao, M. Pasta, H.N. Alshareef, Y. Cui, Symmetrical MnO2-carbon nanotube-textile nanostructures for wearable pseudocapacitors with high mass loading, ACS Nano. 5 (2011) 8904–8913. doi:10.1021/nn203085j.

[122] S.L. Chou, J.Z. Wang, S.Y. Chew, H.K. Liu, S.X. Dou, Electrodeposition of MnO2 nanowires on carbon nanotube paper as free-standing, flexible electrode for supercapacitors, Electrochem. Commun. 10 (2008) 1724–1727. doi:10.1016/j.elecom.2008.08.051.

[123] H. Li, Y. He, V. Pavlinek, Q. Cheng, P. Saha, C. Li, MnO2 nanoflake/polyaniline

nanorod hybrid nanostructures on graphene paper for high-performance flexible supercapacitor electrodes, J. Mater. Chem. A. 3 (2015) 17165–17171. doi:10.1039/C5TA04008F.

[124] Y. Saito, M. Meguro, M. Ashizawa, K. Waki, R. Yuksel, H.E. Unalan, H. Matsumoto, Manganese dioxide nanowires on carbon nanofiber frameworks for efficient electrochemical device electrodes, RSC Adv. 7 (2017) 12351–12358. doi:10.1039/C6RA28789A.

[125] Z. Ye, T. Li, G. Ma, X. Peng, J. Zhao, Morphology controlled MnO2 electrodeposited on carbon fiber paper for high-performance supercapacitors, J. Power Sources. 351 (2017) 51–57. doi:10.1016/j.jpowsour.2017.03.104.

[126] G.K. Ramesha, S. Sampath, Electrochemical Reduction of Oriented Graphene Oxide Films: An in Situ Raman Spectroelectrochemical Study, J. Phys. Chem. C. 113 (2009) 7985–7989. doi:10.1021/jp811377n.

[127] C.M. Julien, M. Massot, C. Poinsignon, Lattice vibrations of manganese oxides Part I . Periodic structures, Spectrochim. Acta. 60 (2004) 689–700. doi:10.1016/S1386-1425(03)00279-8.

[128] S. Ardizzone, C.L. Bianchi, D. Tirelli, Mn3O4 and γ-MnOOH powders, preparation, phase composition and XPS characterisation, Colloids Surfaces A Physicochem. Eng. Asp. 134 (1998) 305–312. doi:10.1016/S0927-7757(97)00219-7.

[129] A.A. Audi, P.M.A. Sherwood, Valence-band x-ray photoelectron spectroscopic studies of manganese and its oxides interpreted by cluster and band structure calculations, Surf. Interface Anal. 33 (2002) 274–282. doi:10.1002/sia.1211.

[130] M. Toupin, T. Brousse, D. Bélanger, Influence of Microstucture on the Charge Storage Properties of Chemically Synthesized Manganese Dioxide, Chem. Mater. 14 (2002) 3946–3952. doi:10.1021/cm020408q.

[131] M. Toupin, T. Brousse, D. Bélanger, Charge Storage Mechanism of MnO 2 Electrode Used in Aqueous Electrochemical Capacitor, Chem. Mater. 16 (2004) 3184–3190. doi:10.1021/cm049649j.

[132] Z. Niu, J. Chen, H.H. Hng, J. Ma, X. Chen, A leavening strategy to prepare reduced graphene oxide foams, Adv. Mater. 24 (2012) 4144–4150. doi:10.1002/adma.201200197.

[133] T. Nguyen, M. João Carmezim, M. Boudard, M. Fátima Montemor, Cathodic electrodeposition and electrochemical response of manganese oxide pseudocapacitor electrodes, Int. J. Hydrogen Energy. 40 (2015) 16355–16364. doi:10.1016/j.ijhydene.2015.10.041.

[134] Q. Cheng, J. Tang, Graphene and nanostructured MnO2 composite electrodes for supercapacitors, Carbon N. Y. 49 (2011) 2917–2925. doi:10.1016/j.carbon.2011.02.068.

[135] D. Wang, Q. Wang, T. Wang, Morphology-Controllable Synthesis of Cobalt Oxalates and Their Conversion to Mesoporous Co3O4 Nanostructures for Application in Supercapacitors, Inorg. Chem. 50 (2011) 6482–6492. doi:10.1021/ic200309t.

[136] D. Wang, Y. Li, Q. Wang, T. Wang, Facile Synthesis of Porous Mn3O4 Nanocrystal – Graphene Nanocomposites for Electrochemical Supercapacitors, Eur. J. Inorg. Chem. (2012) 628–635. doi:10.1002/ejic.201100983.

[137] V. Subramanian, H. Zhu, R. Vajtai, P.M. Ajayan, B. Wei, Hydrothermal Synthesis and Pseudocapacitance Properties of MnO2 Nanostructures, J. Phys. Chem. B. 109 (2005) 20207–20214. doi:10.1021/jp0543330.

[138] G. An, P. Yu, M. Xiao, Z. Liu, Low-temperature synthesis of Mn3O4 nanoparticles loaded on multi-walled carbon nanotubes and their application in electrochemical capacitors, Nanotechnology. 19 (2008) 275709. doi:10.1088/0957-4484/19/27/275709.

[139] C. Julien, M. Massot, R. Baddour-Hadjean, S. Franger, S. Bach, J.P. Pereira-Ramos, Raman spectra of birnessite manganese dioxides, Solid State Ionics. 159 (2003) 345–356. doi:10.1016/S0167-2738(03)00035-3.

[140] N. Nagarajan, H. Humadi, I. Zhitomirsky, Cathodic electrodeposition of MnOx films for electrochemical supercapacitors, Electrochim. Acta. 51 (2006) 3039–3045. doi:10.1016/j.electacta.2005.08.042.

[141] L. Yang, S. Cheng, X. Ji, Y. Jiang, J. Zhou, M. Liu, Investigations into the origin of pseudocapacitive behavior of Mn3O4 electrodes using in operando Raman spectroscopy, J. Mater. Chem. A. 3 (2015) 7338–7344. doi:10.1039/C5TA00223K.

[142] M.K. Song, S. Cheng, H. Chen, W. Qin, K.W. Nam, S. Xu, X.Q. Yang, A. Bongiorno, J. Lee, J. Bai, T.A. Tyson, J. Cho, M. Liu, Anomalous pseudocapacitive behavior of a nanostructured, mixed-valent manganese oxide film for electrical energy storage, Nano Lett. 12 (2012) 3483–3490. doi:10.1021/nl300984y.

[143] Y. Luo, J. Jiang, W. Zhou, H. Yang, J. Luo, X. Qi, H. Zhang, D.Y.W. Yu, C.M. Li, T. Yu, Self-assembly of well-ordered whisker-like manganese oxide arrays on carbon fiber paper and its application as electrode material for supercapacitors, J. Mater. Chem. 22 (2012) 8634–8640. doi:10.1039/c2jm16419a.

[144] M. Sawangphruk, P. Srimuk, P. Chiochan, High-performance supercapacitor of manganese oxide / reduced graphene oxide nanocomposite coated on flexible carbon fiber paper, Carbon N. Y. 60 (2013) 109–116. doi:10.1016/j.carbon.2013.03.062.

[145] J. Yan, Z. Fan, W. Sun, G. Ning, T. Wei, Q. Zhang, R. Zhang, L. Zhi, F. Wei, Advanced asymmetric supercapacitors based on Ni(OH)2/graphene and porous graphene electrodes with high energy density, Adv. Funct. Mater. 22 (2012) 2632–2641. doi:10.1002/adfm.201102839.

[146] Y. Hu, C. Guan, G. Feng, Q. Ke, X. Huang, J. Wang, Flexible asymmetric

supercapacitor based on structure-optimized Mn3O4/reduced graphene oxide nanohybrid paper with high energy and power density, Adv. Funct. Mater. 25 (2015) 7291–7299. doi:10.1002/adfm.201503528.

[147] Y. Gogotsi, P. Simon, Materials for electrochemical capacitors, Nat. Mater. 7 (2008) 845–854.

[148] R.R. Salunkhe, J. Lin, V. Malgras, S. Xue, J. Ho, Y. Yamauchi, Large-scale synthesis of coaxial carbon nanotube / Ni (OH) 2 composites for asymmetric supercapacitor application, Nano Energy. 11 (2015) 211–218. doi:10.1016/j.nanoen.2014.09.030.

[149] J. Piwek, A. Platek, K. Fic, E. Frackowiak, Carbon-based electrochemical capacitors with acetate aqueous electrolytes, Electrochim. Acta. 215 (2016) 179–186. doi:10.1016/j.electacta.2016.08.061.

[150] C.J. Jafta, F. Nkosi, L. le Roux, M.K. Mathe, M. Kebede, K. Makgopa, Y. Song, D. Tong, M. Oyama, N. Manyala, S. Chen, K.I. Ozoemena, Manganese oxide/graphene oxide composites for high-energy aqueous asymmetric electrochemical capacitors, Electrochim. Acta. 110 (2013) 228–233. doi:10.1016/j.electacta.2013.06.096.

[151] J.Y. Hwang, M.F. El-Kady, Y. Wang, L. Wang, Y. Shao, K. Marsh, J.M. Ko, R.B. Kaner, Direct preparation and processing of graphene/RuO2 nanocomposite electrodes for high-performance capacitive energy storage, Nano Energy. 18 (2015) 57–70. doi:10.1016/j.nanoen.2015.09.009.

[152] H. Fan, R. Niu, J. Duan, W. Liu, W. Shen, Fe3O4@Carbon Nanosheets for All-Solid-State Supercapacitor Electrodes, Appl. Mater. Interfaces. 8 (2016) 19475–19483. doi:10.1021/acsami.6b05415.

[153] V.A. Online, In situ growth of monodisperse Fe 3 O 4 nanoparticles on graphene as fl exible paper for, (2014) 12068–12074. doi:10.1039/c4ta01442a.

[154] C. Long, T. Wei, J. Yan, L. Jiang, Z. Fan, Supercapacitors based on graphene-

supported iron nanosheets as negative electrode materials, ACS Nano. 7 (2013) 11325–11332. doi:10.1021/nn405192s.

[155] M. Liu, J. Sun, In situ growth of monodisperse Fe3O4 nanoparticles on graphene as flexible paper for supercapacitor, J. Mater. Chem. A. 2 (2014) 12068–12074. doi:10.1039/C4TA01442A.

[156] Q. Wang, L. Jiao, H. Du, Y. Wang, H. Yuan, Fe 3 O 4 nanoparticles grown on graphene as advanced electrode materials for supercapacitors, J. Power Sources. 245 (2014) 101–106. doi:10.1016/j.jpowsour.2013.06.035.

[157] L. Li, P. Gao, S. Gai, F. He, Y. Chen, M. Zhang, P. Yang, Ultra small and highly dispersed Fe3O4 nanoparticles anchored on reduced graphene for supercapacitor application, Electrochim. Acta. 190 (2016) 566–573. doi:10.1016/j.electacta.2015.12.137.

[158] A.K. Das, S. Sahoo, P. Arunachalam, S. Zhang, J. Shim, Facile synthesis of Fe 3 O 4 nanorod decorated reduced graphene oxide (RGO) for supercapacitor, RSC Adv. 6 (2016) 107057–107064. doi:10.1039/c6ra23665k.

[159] F.E. Sarac Oztuna, O. Unal, E. Erdem, H. Yagci Acar, U. Unal, Layer-by-Layer Grown Electrodes Composed of Cationic Fe3O4 Nanoparticles and Graphene Oxide Nanosheets for Electrochemical Energy Storage Devices, J. Phys. Chem. C. (2019) acs.jpcc.8b11772. doi:10.1021/acs.jpcc.8b11772.

[160] P.C.J. Graat, M.A.J. Somers, Simultaneous determination of composition and thickness of thin iron-oxide films from XPS Fe 2p spectra, Appl. Surf. Sci. 100 (1996) 36–40.

[161] J.M. Lee, M.E. Briggs, C. Hu, A.I. Cooper, Controlling electric double-layer capacitance and pseudocapacitance in heteroatom-doped carbons derived from hypercrosslinked microporous polymers, Nano Energy. 46 (2018) 277–289. doi:10.1016/j.nanoen.2018.01.042.

[162] A. Laheäär, P. Przygocki, Q. Abbas, F. Béguin, Appropriate methods for evaluating the efficiency and capacitive behavior of different types of supercapacitors, Electrochem. Commun. 60 (2015) 21–25. doi:10.1016/j.elecom.2015.07.022.

[163] X. Chen, R. Paul, L. Dai, Carbon-based supercapacitors for efficient energy storage, Natl. Sci. Rev. 4 (2017) 453–489. doi:10.1093/nsr/nwx009.

[164] S. Sun, S. Wang, T. Xia, X. Li, Q. Jin, Q. Wu, L. Wang, Z. Wei, P. Wang, Hydrothermal synthesis of a MnOOH/three-dimensional reduced graphene oxide composite and its electrochemical properties for supercapacitors, J. Mater. Chem. A. 3 (2015) 20944–20951. doi:10.1039/C5TA04851F.

[165] H. Jiang, T. Zhao, C. Li, J. Ma, Hierarchical self-assembly of ultrathin nickel hydroxide nanoflakes for high-performance supercapacitors, J. Mater. Chem. 21 (2011) 3818. doi:10.1039/c0jm03830j.

VITA

Tuğçe Beyazay was born in Istanbul, Turkey in 1992. She graduated from Beşiktaş Atatürk Anatolian high school in 2010. She received her B.Sc. degree in Chemistry from Koç University in 2016. In September 2016, she started her M.Sc. degree in Materials Science and Engineering at Koç University and joined Functional Materials Research Group as a research assistant under supervision of Assoc. Prof. Uğur Ünal.